iScience

CellPress
OPEN ACCESS

Article

Nacreous aramid-mica bulk materials with excellent mechanical properties and environmental stability

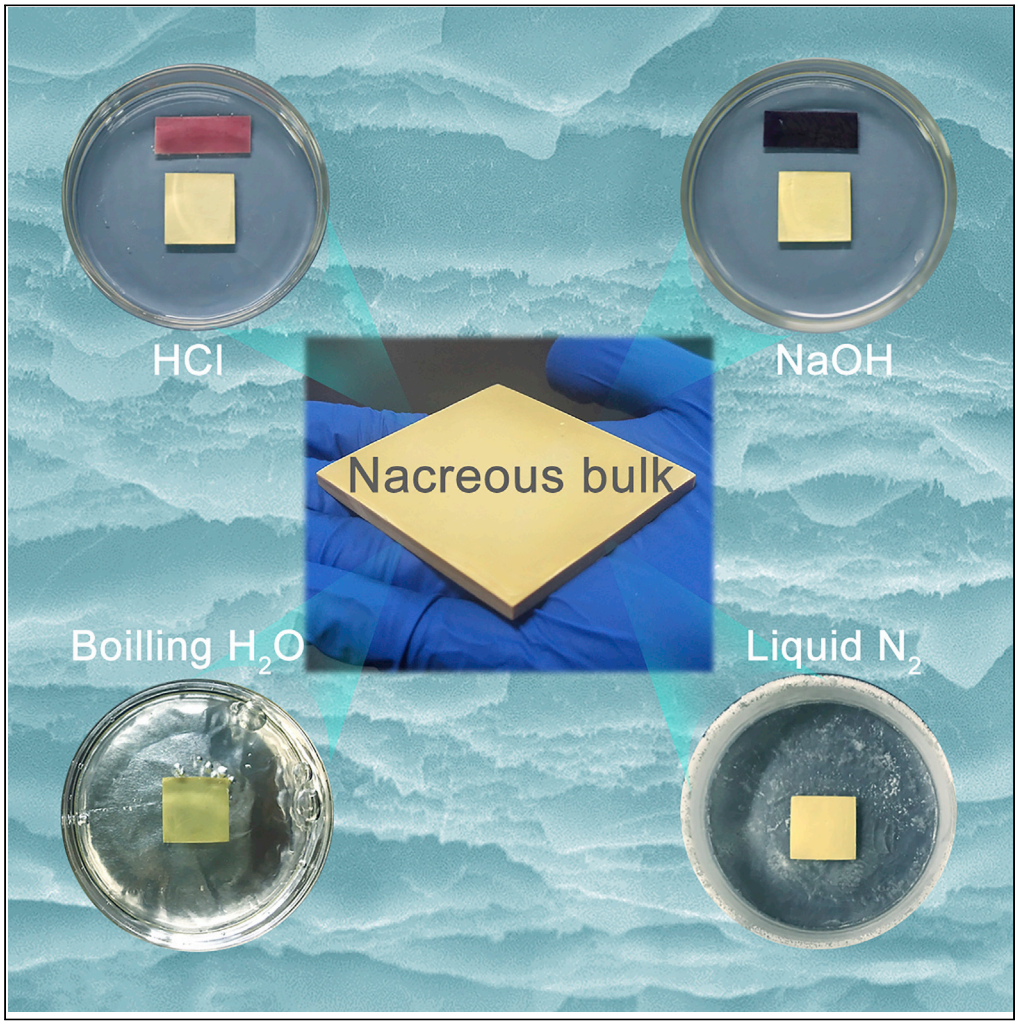

Xiao-Feng Pan, Huai-Ling Gao, Kai-Jin Wu, ..., Yang Lu, Yong Ni, Shu-Hong Yu

yni@ustc.edu.cn (Y.N.)
shyu@ustc.edu.cn (S.-H.Y.)

Highlights

Spray, protonation, evaporation, and lamination techniques are combined

Aramid nanofibers and mica microplatelets are assembled into nacreous bulk

Nacre-inspired design imparts the nacreous bulk with high mechanical performance

Nacreous bulk displays favorable mechanical stability in some harsh environments

Pan et al., iScience *24*, 101971
January 22, 2021
https://doi.org/10.1016/j.isci.2020.101971

iScience

CellPress
OPEN ACCESS

Article

Nacreous aramid-mica bulk materials with excellent mechanical properties and environmental stability

Xiao-Feng Pan,[1,4] Huai-Ling Gao,[1,4] Kai-Jin Wu,[2,4] Si-Ming Chen,[1] Tao He,[3] Yang Lu,[3] Yong Ni,[2,*] and Shu-Hong Yu[1,2,5,*]

Summary

Low density, high strength and toughness, together with good environmental stability are always desirable but hardly to achieve simultaneously for man-made structural materials. Replicating the design motifs of natural nacre clearly provides one promising route to obtain such kind of materials, but fundamental challenges remain. Herein, by choosing aramid nanofibers and mica microplatelets as building blocks, we produce a nacreous aramid-mica bulk material with a favorable combination of low density (~1.7 g cm^{-3}), high strength (~387 MPa) and toughness (~14.3 MPa $m^{1/2}$), and impressive mechanical stability in some harsh environments, including acid/alkali solutions, strong ultraviolet radiation, boiling water, and liquid nitrogen, standing out from previously reported biomimetic bulk composites. Moreover, the obtained material outperforms other bulk nacre-mimetics and most engineering structural materials in terms of its specific strength (227 MPa/[Mg m^{-3}]) and specific toughness (8.4 MPa $m^{1/2}$/[Mg m^{-3}]), making it a new promising engineering structural material for different technical fields.

Introduction

The rapid development of various engineering fields is putting forward increasing requirements for the overall performances, including density, mechanical properties, environmental stability, *etc.*, of structural materials (Ritchie, 2011; Wegst et al., 2015; Yu et al., 2018). In particular, the stability of structural materials applied in many harsh environments, such as extreme temperature, hydrotherm, acid-bases, *etc.*, is indispensable (Yu et al., 2018). Incredibly, nature organisms have found ways to adapt to the complex living environments by evolving a wide range of amazing biological structural materials based on very limited selection of constituents (Barthelat et al., 2016; Eder et al., 2018; Huang et al., 2019). As a presented example, the shell from a deep-sea hydrothermal vent gastropod (*Crysomallon squamiferum*) serves not only as mechanical armor from predators, but also as protection from harsh corrosive and dissolutive marine environments (e.g., brackish, cold-water, low-pH conditions) (Yao et al., 2010). In addition, natural nacre from the shell of mollusk, a typical biological structural material, presents a striking trade-off between strength and toughness owing to its hierarchical layered structure and extrinsic toughening mechanisms across multiple scales (Barthelat et al., 2007; Fratzl and Weinkamer, 2007). The unusual mechanical properties combined with its low density predestine it to be one of the most studied models to be imitated for creating advanced structural materials (Peng and Cheng, 2017; Zhao and Guo, 2017).

To date, great achievements have been made in fabricating nacre-mimetic materials with precise control of their structures at multiple scales aiming to enhance their ultimate mechanical performance (Bouville et al., 2014; Le Ferrand et al., 2015; Mao et al., 2016; Pan et al., 2018; Yang et al., 2019b). Among them, organic-inorganic nacre-mimetic composites with macroscale bulk form have shown great potential as lightweight load-bearing structural materials for diverse engineering fields, such as biomedicine, aerospace, military and automotive industries, due to their low density, high specific strength, and high specific toughness (Du et al., 2019; Gao et al., 2017; Magrini et al., 2019; Yin et al., 2019). However, the overall performances of these composite materials are fundamentally restricted by the intrinsic properties of the organic components. For example, some water-soluble polymers, including polyvinyl alcohol (Chen et al., 2019) and sodium alginate (Gao et al., 2017), are commonly used as organic matrixes in nacre-mimetic composites, but this kind of polymers are very sensitive to humidity, making the relevant composites very unstable when

[1]Division of Nanomaterials & Chemistry, Hefei National Laboratory for Physical Sciences at the Microscale, Institute of Energy, Hefei Comprehensive National Science Center, CAS Center for Excellence in Nanoscience, Department of Chemistry, Institute of Biomimetic Materials & Chemistry, University of Science and Technology of China, Hefei 230026, China

[2]CAS Key Laboratory of Mechanical Behavior and Design of Materials, Department of Modern Mechanics, University of Science and Technology of China, Hefei 230026, China

[3]School of Chemistry and Chemical Engineering, Hefei University of Technology, Hefei 230009, China

[4]These authors contributed equally

[5]Lead contact

*Correspondence: yni@ustc.edu.cn (Y.N.), shyu@ustc.edu.cn (S.-H.Y.)

https://doi.org/10.1016/j.isci.2020.101971

subjected to high humidity and water environments. Other commonly used polymers, such as polyurethanes (Podsiadlo et al., 2009), epoxy (Zhao et al., 2016), and polymethyl methacrylate (Bai et al., 2016), are impervious to water, but their thermal stability and mechanical properties are still unsatisfying, largely limiting their practical applications. Overall, it remains challenging to produce organic-inorganic nacre-mimetic bulk materials with desirable combination of lightweight, high strength, high toughness, and good mechanical stability in adverse environments.

Aramid macrofibers, commonly known as Kevlar, are attractive for their low density (1.44 g cm^{-3}), high tensile strength (~3.6 GPa) and stiffness (~109 GPa), chemical resistance, and thermal stability (Xu et al., 2018). Aramid nanofibers (ANFs) are solution-processable nanoscale versions of Kevlar. As a new type of polymer nanofibers recently developed, ANFs not only retain exceptional intrinsic properties of their macroscale parent but also gain certain unique characteristics due to their nanoscale morphology (Yang et al., 2020). In the meantime, mica microplatelets, a kind of rich and cheap natural silicate mineral, also have attractive property combination of low density (~2.8 g cm^{-3}) (Perez-Rodriguez et al., 2006), high mechanical performance (tensile strength ~420 MPa, modulus ~13.2 GPa), chemical and thermal durability, as well as unique ultraviolet (UV)-shielding property (Pan et al., 2018). These characteristics make ANFs and mica microplatelets ideal organic and inorganic building blocks, respectively, for assembling nacreous layered structure materials.

Herein, by hierarchically integrating ANFs and mica microplatelets together, we successfully produce a new-style organic-inorganic nacreous bulk material (nacreous ANFs-Mica bulk) with simultaneous achievement of low density, high strength and toughness, as well as excellent stability to some harsh environments. It was fabricated via a highly efficient bottom-up strategy proposed here, which combines spray-assisted gelation, solvent exchange, evaporation-induced self-assembly and further lamination (Gao et al., 2017) procedures. By optimizing the component proportion and the interfaces from nanoscale to macroscale, the resultant nacreous ANFs-Mica bulk (containing 40 wt.% of mica) not only exhibits low density (~1.7 g cm^{-3}) but also possesses high strength (~387 MPa), stiffness (~18.3 GPa), and fracture toughness (~14.3 MPa $m^{1/2}$), surpassing those of many existing biomimetic bulk composites. Notably, both its specific strength (σ_f/ρ) and specific toughness (K_c/ρ) are higher than those of previously reported bulk nacre-mimetics, and most traditional engineering structural materials. In particular, the mechanical properties of the nacreous ANFs-Mica bulk can keep stable in a series of adverse environments, including acid and alkali solutions, boiling water, liquid nitrogen, and strong UV radiation.

Results and discussion

Fabrication and environmental stability

Aramid macrofibers were first split into high-quality ANFs by deprotonation (Figure S1) in saturated potassium hydroxide dimethyl sulfoxide (DMSO) solution (Xu et al., 2018). In order to enhance interfacial interaction between mica and ANFs via forming hydrogen bonds (Kim et al., 2014; Yang et al., 2015), mica microplatelets were modified with polyacrylic acid (PAA) on their surface (Figure S2). Afterward, ANFs serving as organic matrix and PAA modified mica microplatelets (PAA-mica) serving as inorganic bricks were assembled together to fabricate nacreous ANFs-Mica films at first via a spray-assisted gelation, solvent exchange and further evaporation processes we proposed here (Figures 1A–1C). In brief, the ANFs-Mica dispersion was sprayed onto a glass plate at room temperature, which quickly turned into gel (Figures 1A, S3A, and S3B) via seizing protons from water vapor in the air (protonation) during this process (Xu et al., 2018). The spray-assisted gelation method developed in this work allowed us to quickly obtain a homogeneous ANFs-Mica-DMSO-H_2O gel with controllable thickness according to the volumes of the sprayed dispersion. Subsequently, in order to further restore the molecular structure of the ANFs by protonation (Yang et al., 2019a), the ANFs-Mica-DMSO-H_2O gel was immersed into deionized water (DIW) to exchange DMSO, forming an ANFs-Mica-H_2O gel (Figures 1B, S3C, and S3D). Then, the expected nacreous ANFs-Mica film could be obtained by drying this hydrogel via evaporating its containing DIW (Figures S3E and S3F). It was supposed that mica microplatelets embedded in the hydrogel were gradually organized in parallel to each other along the surface direction during this evaporation process (Ji et al., 2018), resulting in the typical nacreous "bricks-and-mortar" microstructure (Figure 1C). These films were further cut with equal size, modified with 3-(trimethoxysilyl) propyl methacrylate (γ-MPS) and laminated together with epoxy resin as the interfacial adhesive among the films, forming the expected nacreous ANFs-Mica bulk with desired size (Figure 1D). Fracture morphology of the nacreous ANFs-Mica bulk displayed a typical step-like layered microstructure (Figures 1D and S4), closely resembling that of natural nacre.

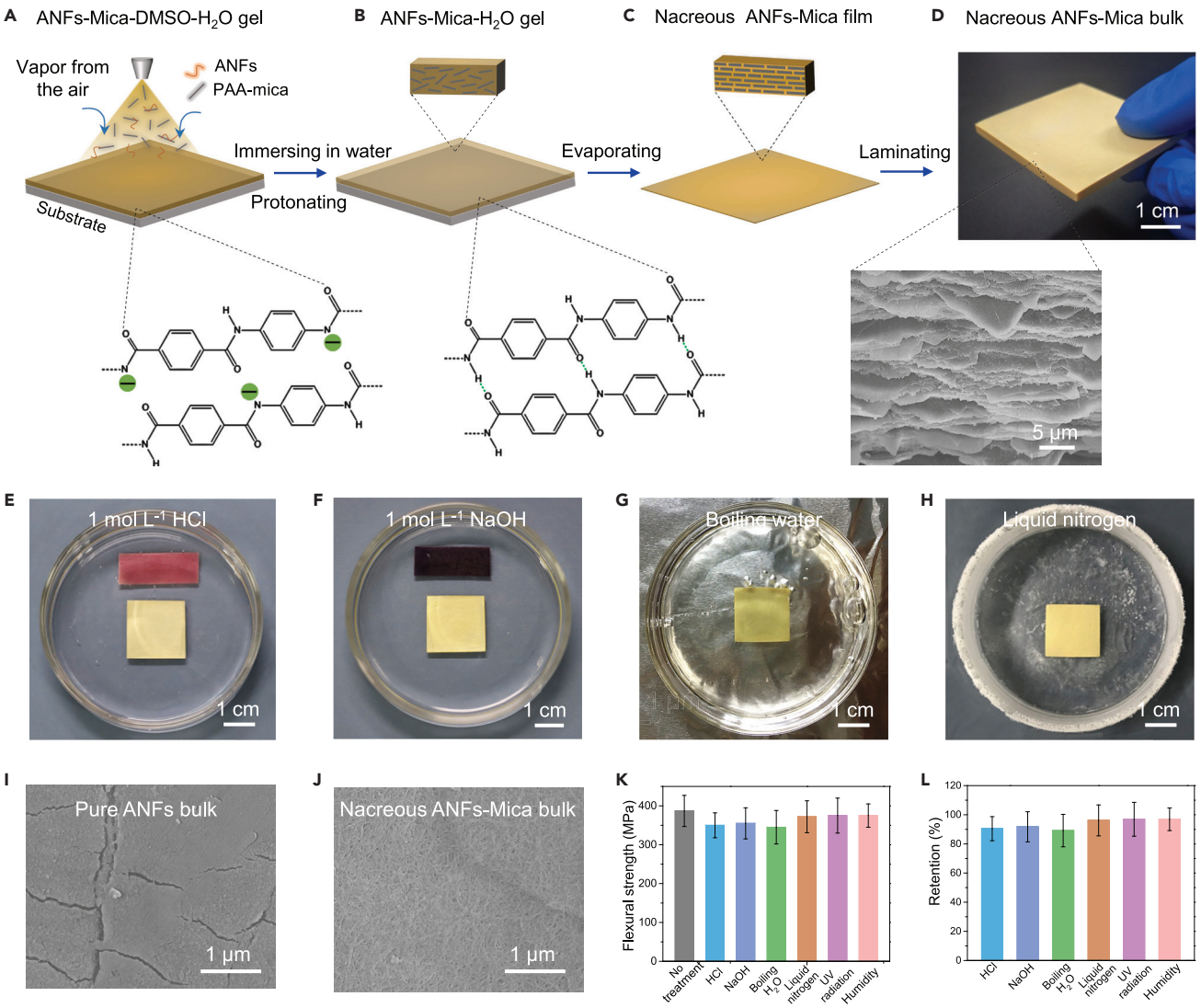

Figure 1. Fabrication of the nacreous ANFs-Mica bulk and its environmental stability

(A–D) Schematic diagram showing the fabrication process of the nacreous ANFs-Mica bulk (40 wt.%). It is assembled from ANFs and mica microplatelets via a mild and scalable bottom-up strategy which combines spray-assisted gelation (A), protonation by solvent exchange (B), evaporation-induced self-assembly (C) and further lamination (D) together.

(E–H) Photographs of the nacreous ANFs-Mica bulk (40 wt.%) immersed into 1 mol L^{-1} HCl solution, 1 mol L^{-1} NaOH solution, boiling water and liquid nitrogen, respectively.

(I and J) Surface SEM images of the pure ANFs bulk and nacreous ANFs-Mica bulk (40 wt.%) after treatment by UV radiation (6 days), respectively.

(K and L) Flexural strength and its retention of the nacreous ANFs-Mica bulk (40 wt.%), respectively, after treatment by 1 mol L^{-1} HCl solution (24 hr), 1 mol L^{-1} NaOH solution (24 hr), boiling water (24 hr), liquid nitrogen (24 hr), UV radiation (6 days) and 80% relative humidity (RH) (24 hr). Error bars manifest standard deviation (s.d.) of at least six measurements.

See also Figures S1–S6, and Videos S1 and S2

As we expected, the obtained nacreous ANFs-Mica bulk exhibits a good structural and mechanical stability when exposed to several typical harsh environments (Figures 1E–1J, and Videos S1 and S2). We found that the specimens maintained their integrity with invisible morphology change when immersing in acid (1 mol L^{-1} HCl) and alkali (1 mol L^{-1} NaOH) solutions, boiling water as well as liquid nitrogen, respectively (Figures 1E–1H). In addition, in contrast to the pure ANFs bulk materials with many microcracks and etching on its surface after exposure to strong UV radiation, the nacreous ANFs-Mica bulk did not show any microstructural change (Figures 1I, 1J, and S5). Further mechanical testing revealed that flexural strength of these specimens still kept at high values and shown slight decreases (Figures 1K and 1L). To be noted, the

nacreous ANFs-Mica bulk revealed much better mechanical stability than that of pure ANFs bulk materials (Figure S6). These experimental results indicate the excellent environmental stability of the prepared nacreous ANFs-Mica bulk, which is elusive for many previously reported organic-inorganic nacre-mimetic composites.

Structural and mechanical characterizations

The superior mechanical properties and stability of the nacreous ANFs-Mica bulk in adverse environments can be mainly attributed to the intrinsic merits of the utilized building blocks and the hierarchically structural design. After assembling the two kinds of nanoscale building blocks into nacreous ANFs-Mica films (Figure S7), their intrinsic merits were supposed to be successfully integrated together and transferred to the ANFs-Mica films. The cross-sectional morphology of the ANFs-Mica films shows typical nacreous layered structure (Figures 2A and S8), which was formed via evaporation-induced self-assembly of the building blocks during the drying process of the ANFs-Mica hydrogels (Ji et al., 2018). Moreover, the ANFs-Mica film (40 wt.%) with different thicknesses could be easily fabricated by adjusting the thickness of the deposited gels (Figure S9). The ANFs-Mica film with optimized mechanical enhancement was confirmed to have 40 wt.% of mica microplatelets. The optimal tensile strength, toughness, and Young's modulus were measured to be approximately 220 MPa, 21 MJ m^{-3}, and 9.2 GPa, respectively, which were all much higher than those of the pure ANFs films (Figures 2B and S10). These obvious mechanical enhancements were predominantly ascribed to the efficient interfacial interaction between PAA-mica and ANFs mediated by hydrogen bonding at molecular level (Figure S11), and the nacreous layered structure at nano/microlevel (Peng and Cheng, 2017). Theoretical analysis further displayed that there existed an optimum volume fraction of mica microplatelets that maximize the strength and toughness of the nacreous ANFs-Mica film (Figure S12), which is consistent with the experimental investigations. In addition, experimental results demonstrated that the nacreous ANFs-Mica films retained at least 93% of their original tensile strength after stored at a relative high temperature ($\leq$250°C) for 6 hr, outperforming that of pure ANFs films treated with same conditions (Figures 2C and S13). These results indicate that the intrinsic high thermal stability of both mica and ANFs (Hepburn et al., 2000; Xu et al., 2018) contributes to the satisfactory thermal stability of the nacreous ANFs-Mica film. Additionally, the visible transmittance of the resultant films displayed slow reduction with an increasing mica content, whereas their UV transmittance was all completely shielding (Figure 2D) due to the strong UV absorption capacity of ANFs (Patterson and Sodano, 2016). This intrinsic optical property of ANFs commonly causes the decomposition of their molecular chains (Patterson and Sodano, 2016), namely UV aging. Notably, owing to the intrinsic UV-shielding property of mica (Pan et al., 2018), the UV absorbance of those nacreous ANFs-Mica films was enhanced with an increasing mica content (Figure 2E). Therefore, mechanical performance of the nacreous ANFs-Mica film containing 40 wt.% of mica was more stable than that of the pure ANFs film when exposed to strong UV radiation (Figures 2F and S14). These experimental results manifest that the intrinsic mechanical, thermal and chemical properties of mica and ANFs, together with the unique UV-shielding property of mica were successfully integrated into the obtained nacreous films.

The nacreous ANFs-Mica films with integrated properties were then used as the second-level building blocks to construct the nacreous bulk materials. The fracture surface of the obtained ANFs-Mica bulk exhibits a similar nacreous layered structure at larger length scale compared with that of nacreous ANFs-Mica film (Figures 3A and S15A), and no delamination or cavity was observed (Figure S15B). This result reveals that the laminating procedure did not perturb the ordered structure of these films, while compact these ANFs-Mica films into one dense unity. After further optimizing the preparation conditions (Figure S16), the ultimate flexural strength and stiffness of the nacreous ANFs-Mica bulk reached ~387 MPa and ~18.3 GPa (Figures 3B and 3C), respectively. The fracture toughness, K_{IC}, as an evaluation of the resistance to a crack initiation, was tested to be ~4.9 MPa $m^{1/2}$ (Figure 3D). In addition, its maximum fracture toughness, K_{JC}, of the nacreous ANFs-Mica bulk increased by more than two times from the crack initiation (~4.9 MPa $m^{1/2}$) to the end of the stable crack propagation (~14.3 MPa $m^{1/2}$) (Figures 3D and 3E). These mechanical properties are all higher than those of the pure ANFs bulk, the disordered ANFs-Mica composite (Figure S15C), the nacreous ANFs-Mica bulk assembled from mica microplatelets without PAA modification, as well as the nacreous ANFs-Mica bulk assembled from ANFs-Mica films without γ-MPS modification (Figures 3C–3E). Furthermore, Vickers hardness of the nacreous ANFs-Mica bulk (~68 kg mm^{-2}) was also distinctly improved relative to the pure ANFs bulk (~40 kg mm^{-2}) (Figure S17). These mechanical enhancements greatly certify the validity of the hierarchically structural design at multiple scales presented here.

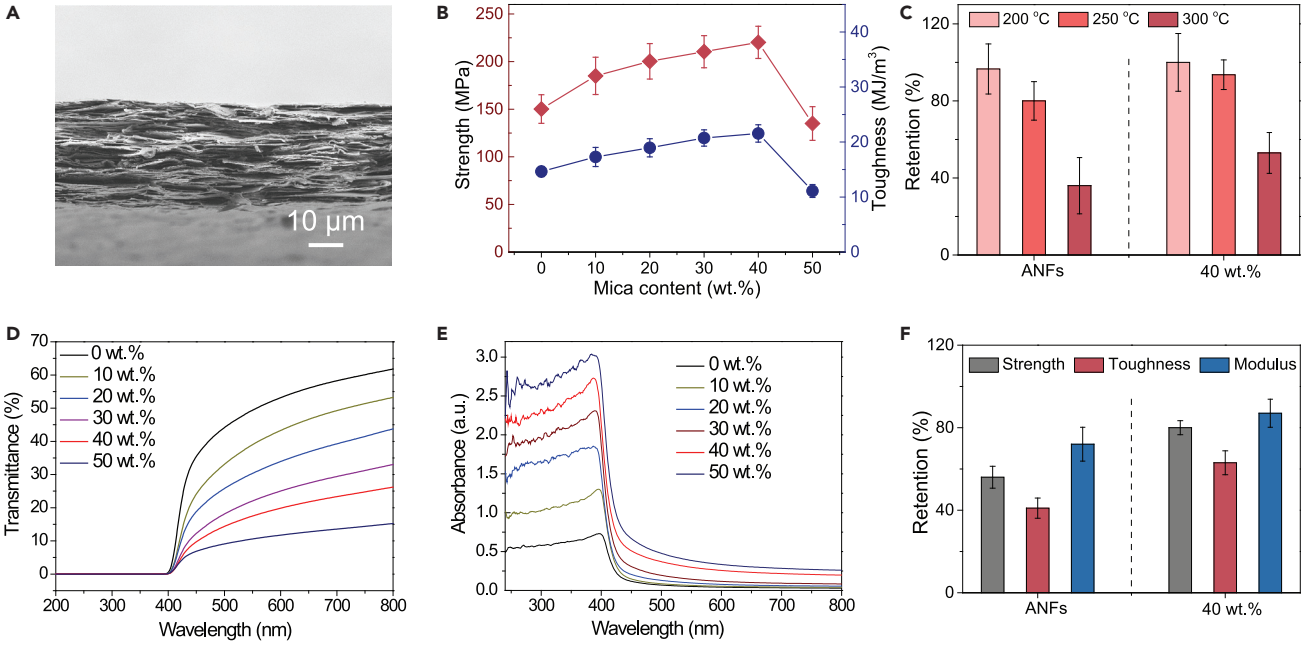

Figure 2. Characterization of nacreous ANFs-Mica films

(A) Cross-sectional SEM image of the nacreous ANFs-Mica film containing 40 wt.% mica.

(B) Tensile mechanical properties (strength and toughness) of the nacreous ANFs-Mica films with different mica contents.

(C) Retention of tensile strength of the 40 wt.% nacreous ANFs-Mica film and the pure ANFs film after 200°C, 250°C and 300°C treatment for 6 hr, respectively.

(D and E) UV-visible transmittance and absorption spectra of ~30 μm thick ANFs-Mica films with different mica contents.

(F) Retention of mechanical properties of the nacreous ANFs-Mica film containing 40 wt.% mica and the pure ANFs film, respectively, after treatment by UV radiation (6 days). Error bars manifest s.d. of at least six measurements.

See also Figures S7–S14.

Toughening mechanisms analysis

Representative crack-resistance curve (*R*-curve) of the nacreous ANFs-Mica bulk exhibited an analogous extensive rising *R*-curve behavior as that of natural nacre (Figure 3E), indicating the increasing fracture resistance of the nacreous ANFs-Mica bulk during crack propagation (Huang et al., 2019). Multiscale mechanical analysis based on crack-bridging model (Budiansky and Amazigo, 1989; Shao et al., 2012) and finite element (FE) analyses further revealed that the interfacial hydrogen bonds between ANFs and mica microplatelets play a pivotal role in the toughening of the nacreous ANFs-Mica bulk (Figures 3E–3L and S18, and Table S1). Based on the experimental investigations and the FE simulations below (Figures 3I–3L), mica microplatelets were pulled out at the front tip of the crack during the crack propagation process, leading to the formation of crack-bridging zone (Figure 3F) (Budiansky and Amazigo, 1989; Shao et al., 2012). As shown in Figure 3G, hydrogen bonds are formed between NH and CO groups of adjacent ANFs chains, and also between ANFs chains and the COOH group on the surface of PAA-mica (Figure S11). As the mica microplatelets begin to slide relative to each other, hydrogen bonds networks between the neighboring platelets can facilely reform after bond breaking due to micaplatelets and interfibers sliding, which improves the interfacial strength and thus result in much enhanced fracture toughness (Figure 3H). The above toughening mechanisms are consistent with previous researches on toughening staggered layered structures by hydrogen bonds interactions (Zhu et al., 2015). In addition, it is worth mentioning that there also exists other interface dominated toughening mechanisms such as micocrack deflection, crack branching, multiple cracking *etc.*, during crack propagation in the nacreous ANFs-Mica bulk, which could be illustrated by the following experimental observations. As shown in Figures 3I–3K, the multiple extrinsic toughening mechanisms acting at different length scales are clearly displayed. Figure 3I shows that the crack in the nacreous ANFs-Mica bulk initiated from the notch and propagated along a characteristic tortuous path, improving interfacial area per unit crack length. Higher-magnification SEM images of the fracture surface further illustrate the presence of crack branching, multiple cracking and crack bridging at the crack tip (Figure S19 and Video S3). Moreover, a typical trapezoidal fracture surface containing abundant pull-outs of mica microplatelets on the fracture surface and extensive delamination of ANFs-Mica interface were

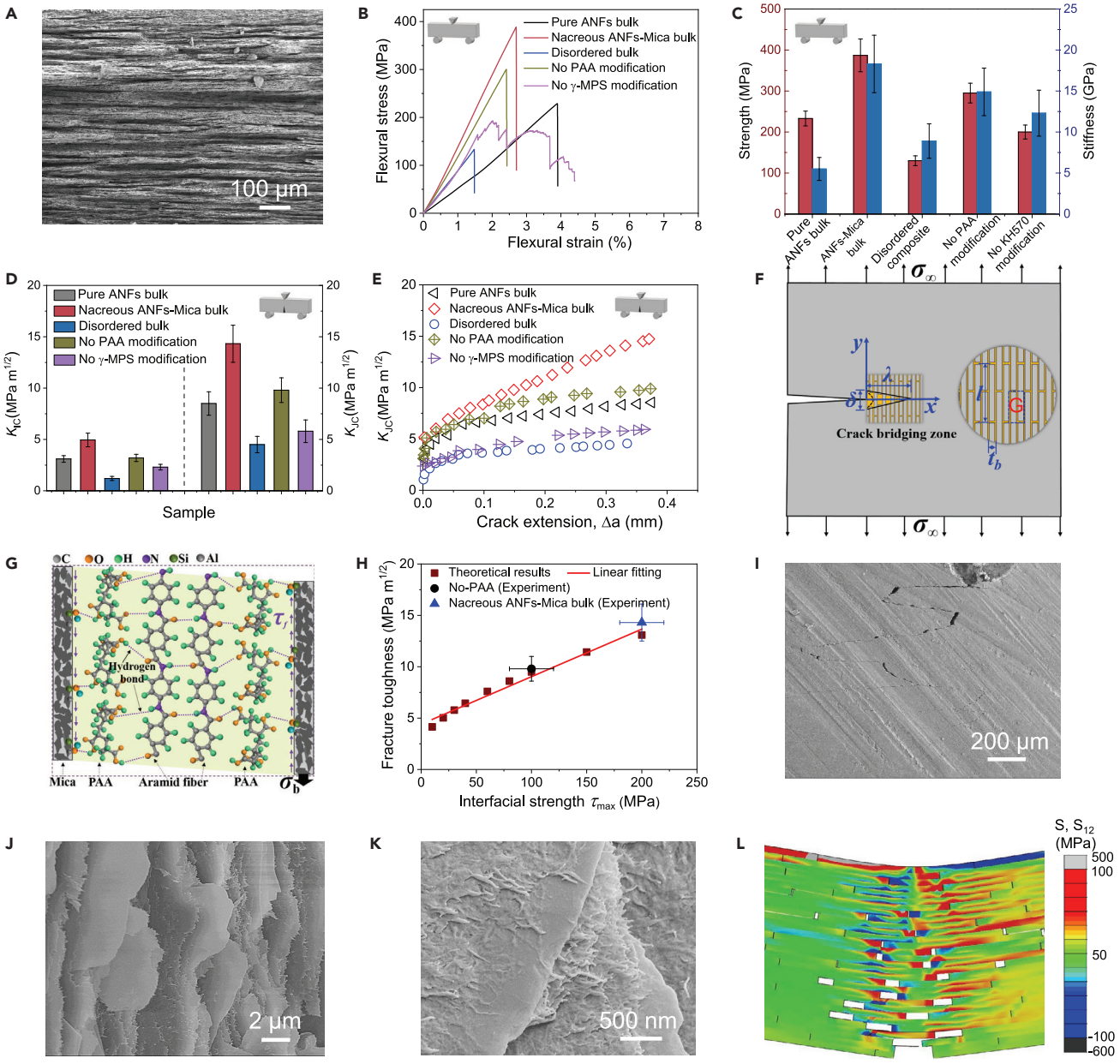

Figure 3. Mechanical performance and multiple extrinsic toughening mechanisms of the nacreous ANFs-Mica bulk

(A) Cross-sectional SEM image of the 40 wt.% nacreous ANFs-Mica bulk.

(B) Flexural stress-strain curves of the 40 wt.% nacreous ANFs-Mica bulk prepared under different conditions of interfacial modification, the pure ANFs bulk and the disordered ANFs-Mica bulk.

(C–E) Comparison of flexural strength and stiffness (C), fracture toughness (D), and representative *R*-curves (E), respectively, of the nacreous ANFs-Mica bulk prepared under different conditions of interfacial modification, the pure ANFs bulk and the disordered ANFs-Mica bulk.

(F) Schematic of the crack-bridging model for the nacreous ANFs-Mica bulk with "brick-and-mortar" microstructure.

(G) Molecular structure of Si-OH group from mica, PAA and ANFs, as well as interfacial hydrogen bond networks formed in the neighboring ANFs and PAA-mica.

(H) Comparison of calculated fracture toughness under different interfacial strength based on mechanical model, the experimental measured fracture toughness for no PAA modified bulk (without hydrogen bonds), and the nacreous ANFs-Mica bulk (with hydrogen bonds).

(I–K) SEM images with different magnifications showing the fracture surfaces of the nacreous ANFs-Mica bulk.

(L) The shear stress field distributions show the progressive interface failure included interlayer sliding, cracking bridging and crack deflection based on FE simulation. Error bars manifest s.d. of at least six measurements.

See also Figures S11 and S15–S20, Table S1 and Videos S3 and S4.

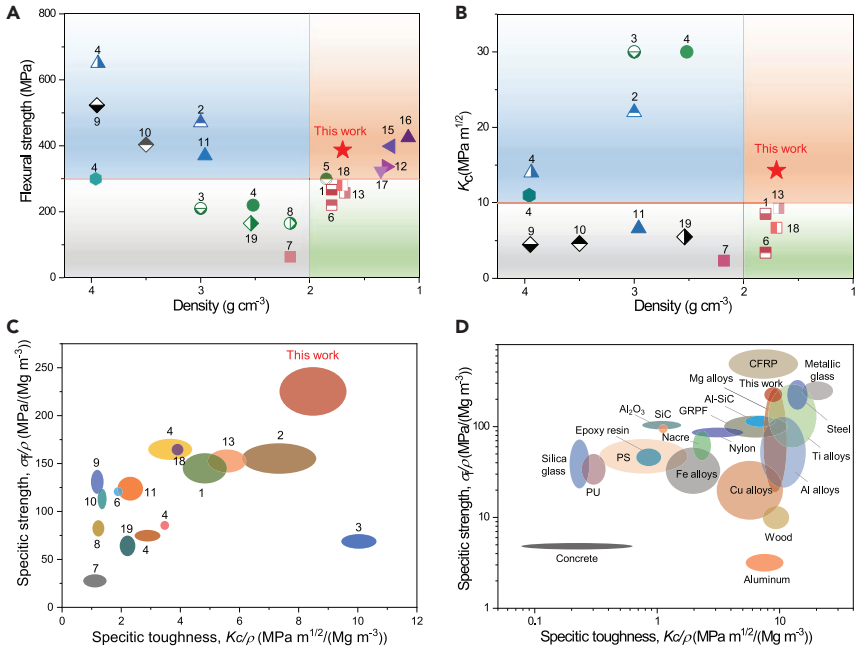

Figure 4. Comparison of mechanical performance of the nacreous ANFs-Mica bulk with relevant bulk structural materials

(A) Ashby chart plotting flexural strength versus density for our nacreous ANFs-Mica bulk and other biomimetic bulk composites.

(B) Ashby chart plotting fracture toughness versus density of our nacreous ANFs-Mica bulk and other biomimetic bulk composites.

(C and D) Ashby diagrams plotting the specific toughness versus specific strength for our nacreous ANFs-Mica bulk compared with other nacre-mimetic bulk composites (C), as well as natural and engineering structural materials (D). Numbers in the charts stand for relevant references in Table S2.

See also Table S2.

observed (Figure 3J). Notably, ANFs layer densely adhered on the surface of mica microplatelets (Figure 3K), indicating strong ANFs-Mica interfacial interaction. These typical multiple extrinsic toughening mechanisms, derived from the hierarchically layered architecture, synergistically dissipated a tremendous amount of mechanical energy at different length scales, leading to an obvious toughness enhancement of the nacreous ANFs-Mica bulk (Bouville et al., 2014; Gao et al., 2017). A three-dimensional (3D) FE simulation was further developed to determine the mechanisms responsible for the mechanical enhancement of the nacreous hierarchical structure. As we expected, similar mechanisms, including interlayer sliding, cracking bridging and crack deflection, as the experiment observed, were also clarified and visualized by the FE simulation (Figures 3L and S20, and Video S4).

With regard to structural materials, besides mechanical properties and environmental stability, density is another main factor, determining their practical applications[1]. Based on the low density of both the building blocks and the designed hierarchical nacreous structure, the nacreous bulk material achieved a striking trade-off among density, strength and toughness, which is hard to accomplish simultaneously for engineering structural materials and demonstrates impressive superiority compared with previously reported biomimetic bulk materials (Figures 4A and 4B) (Bouville et al., 2014; Chen et al., 2018; Estili et al., 2012; Gao et al., 2017; Grossman et al., 2017; Guan et al., 2020a, 2020b; Le Ferrand et al., 2015; Libanori et al., 2013; Liu et al., 2013; Mao et al., 2016; Morits et al., 2017; Munch et al., 2008; Naglieri et al., 2015; Nakagaito et al., 2005; Song et al., 2018; Yang et al., 2017; Zhao et al., 2016). As shown in Figure 4C and Table S2, the specific strength, σ_f/ρ (227 MPa/(Mg m^{-3})) and specific toughness, K_c/ρ (8.4 MPa m$^{1/2}$/(Mg m^{-3})) of our nacreous bulk material are both higher than those of the other bulk nacre-mimetics (Bouville et al., 2014; Chen et al., 2018; Estili et al., 2012; Gao et al., 2017; Grossman et al., 2017; Guan et al., 2020a; Le Ferrand et al., 2015; Libanori et al., 2013; Liu et al., 2013; Mao et al., 2016; Morits et al., 2017; Munch et al., 2008; Naglieri et al., 2015) (Song et al., 2018). Notably, both the σ_f/ρ and K_c/ρ of our nacreous bulk material

are higher than those of nearly all biological structural materials and most engineering structural materials including high-performance ceramics, metallic alloys and even glass-fiber-reinforced polymers (Figure 4D and Table S2) (Bouville et al., 2014; Estili et al., 2012; Gao et al., 2017). Consequently, the nacreous ANFs-Mica bulk presented here is confirmed to be a typical new-style lightweight, strong, tough, and environmentally stable structural material.

Conclusion

In conclusion, a high-performance nacreous bulk material was facilely produced via a mild and scalable bottom-up assembly strategy. Based on the hierarchically structural design and the superior intrinsic properties of the utilized building blocks, the obtained nacreous ANFs-Mica bulk exhibits an impressive combination of low density (1.7 g cm^{-3}), high strength (387 MPa), and high fracture toughness (14.3 MPa $m^{1/2}$). In particular, its mechanical properties can maintain stable in several typical adverse environments, including acid and alkali solutions, boiling water, liquid nitrogen, and strong UV radiation. With respect to its overall property combinations, the nacreous ANFs-Mica bulk possesses great superiority compared with biological structural materials, currently existing bulk nacre-mimetic composites and most engineering structural materials. As a new-style biomimetic structural material, this nacreous ANFs-Mica bulk is expected to offer an applicable choice as a brand new structural material for application in some adverse environments.

Limitations of the study

Nacreous aramid-mica bulk materials with excellent mechanical properties and environmental stability were fabricated under laboratory conditions, but its larger scale preparation still needs to be further investigated.

Resource availability

Lead contact

Further information and requests for resources and reagents should be directed to and will be fulfilled by the Lead Contact, S.-H. Y. (Email: shyu@ustc.edu.cn).

Materials availability

This study did not generate new unique reagents.

Data and code availability

All relevant data are available from the authors upon request.

Methods

All methods can be found in the accompanying Transparent methods supplemental file.

Supplemental information

Supplemental information can be found online at https://doi.org/10.1016/j.isci.2020.101971.

Acknowledgments

This work was supported by the National Natural Science Foundation of China (Grants 21975241, 51732011, 51702310, 21431006, 21761132008), the Foundation for Innovative Research Groups of the National Natural Science Foundation of China (Grant 21521001), Key Research Program of Frontier Sciences, CAS (Grant QYZDJ-SSW-SLH036), the Users with Excellence and Scientific Research Grant of Hefei Science Center of CAS (2015HSC-UE007), the University Synergy Innovation Program of Anhui Province (GXXT-2019-028), the Anhui Provincial Natural Science Foundation (1808085ME115), and the Fundamental Research Funds for the Central Universities (WK2480000005).

Author contributions

S.-H.Y., H.-L.G. and X.-F.P. conceived the idea and designed the experiments. S.-H.Y. supervised the research. X.-F.P. and H.-L.G performed the experiments and analyzed the data. S.-M.C., T.H. and Y.L. helped characterizations and provided valuable advice. Y.N. and K.-J.W. performed the mechanical

analysis of toughening mechanism and mechanical simulations. X.-F.P., H.-L.G, K.-J.W., Y.N. and S.-H.Y. co-wrote the manuscript. All authors discussed the results.

Declaration of interests

The authors declare no competing interests.

Received: October 18, 2020
Revised: December 1, 2020
Accepted: December 16, 2020
Published: January 22, 2021

References

Bai, H., Walsh, F., Gludovatz, B., Delattre, B., Huang, C., Chen, Y., Tomsia, A.P., and Ritchie, R.O. (2016). Bioinspired hydroxyapatite/poly (methyl methacrylate) composite with a nacre-mimetic architecture by a bidirectional freezing method. Adv. Mater. *28*, 50–56.

Barthelat, F., Tang, H., Zavattieri, P.D., Li, C.M., and Espinosa, H.D. (2007). On the mechanics of mother-of-pearl: a key feature in the material hierarchical structure. J. Mech. Phys. Sol. *55*, 306–337.

Barthelat, F., Zhen, Y., and Buehler, M.J. (2016). Structure and mechanics of interfaces in biological materials. Nat. Rev. Mater. *1*, 16007.

Bouville, F., Maire, E., Meille, S., Van de Moortele, B., Stevenson, A.J., and Deville, S. (2014). Strong, tough and stiff bioinspired ceramics from brittle constituents. Nat. Mater. *13*, 508–514.

Budiansky, B., and Amazigo, J.C. (1989). Toughening by aligned, frictionally constrained fibers. J. Mech. Phys. Sol. *37*, 93–109.

Chen, S.M., Gao, H.L., Sun, X.H., Ma, Z.Y., Ma, T., Xia, J., Zhu, Y.B., Zhao, R., Yao, H.B., Wu, H.A., et al. (2019). Superior biomimetic nacreous bulk nanocomposites by a multiscale soft-rigid dual-network interfacial design strategy. Matter *1*, 412–427.

Chen, S.M., Gao, H.L., Zhu, Y.B., Yao, H.B., Mao, L.B., Song, Q.Y., Xia, J., Pan, Z., He, Z., Wu, H.A., et al. (2018). Biomimetic twisted plywood structural materials. Natl. Sci. Rev. *5*, 703–714.

Du, G.L., Mao, A.R., Yu, J.H., Hou, J.J., Zhao, N.F., Han, J.K., Zhao, Q., Gao, W.W., Xie, T., and Bai, H. (2019). Nacre-mimetic composite with intrinsic self-healing and shape-programming capability. Nat. Commun. *10*, 800.

Eder, M., Amini, S., and Fratzl, P. (2018). Biological composites-complex structures for functional diversity. Science *362*, 543–547.

Estili, M., Kawasaki, A., and Sakka, Y. (2012). Highly concentrated 3D macrostructure of individual carbon nanotubes in a ceramic environment. Adv. Mater. *24*, 4322–4326.

Fratzl, P., and Weinkamer, R. (2007). Nature's hierarchical materials. Prog. Mater. Sci. *52*, 1263–1334.

Gao, H.L., Chen, S.M., Mao, L.B., Song, Z.Q., Yao, H.B., Cölfen, H., Luo, X.S., Zhang, F., Pan, Z., Meng, Y.F., et al. (2017). Mass production of bulk artificial nacre with excellent mechanical properties. Nat. Commun. *8*, 287.

Grossman, M., Bouville, F., Erni, F., Masania, K., Libanori, R., and Studart, A.R. (2017). Mineral nano-interconnectivity stiffens and toughens nacre-like composite materials. Adv. Mater. *29*, 1605039.

Guan, Q.F., Yang, H.B., Han, Z.M., Ling, Z.C., and Yu, S.H. (2020a). An all-natural bioinspired structural material for plastic replacement. Nat. Commun. *11*, 5401.

Guan, Q.F., Yang, H.B., Han, Z.M., Zhou, L.C., Zhu, Y.B., Ling, Z.C., Jiang, H.B., Wang, P.F., Ma, T., Wu, H.A., et al. (2020b). Lightweight, tough, and sustainable cellulose nanofiber-derived bulk structural materials with low thermal expansion coefficient. Sci. Adv. *6*, eaaz1114.

Hepburn, D.M., Kemp, I.J., and Shields, A.J. (2000). Mica. IEEE Electr. Insul. Mag. *16*, 19–24.

Huang, W., Restrepo, D., Jung, J.Y., Su, F.Y., Liu, Z.Q., Ritchie, R.O., McKittrick, J., Zavattieri, P., and Kisailus, D. (2019). Multiscale toughening mechanisms in biological materials and bioinspired designs. Adv. Mater. *31*, 1901561.

Ji, D., Choi, S., and Kim, J. (2018). A hydrogel-film casting to fabricate platelet-reinforced polymer composite films exhibiting superior mechanical properties. Small *14*, 1801042.

Kim, Y.S., Li, Y.C., Pitts, W.M., Werrel, M., and Davis, R.D. (2014). Rapid growing clay coatings to reduce the fire threat of furniture. ACS Appl. Mater. Interfaces *6*, 2146–2152.

Le Ferrand, H., Bouville, F., Niebel, T.P., and Studart, A.R. (2015). Magnetically assisted slip casting of bioinspired heterogeneous composites. Nat. Mater. *14*, 1172–1179.

Libanori, R., Erb, R.M., and Studart, A.R. (2013). Mechanics of platelet-reinforced composites assembled using mechanical and magnetic stimuli. ACS Appl. Mater. Interfaces *5*, 10794–10805.

Liu, J., Yan, H., and Jiang, K. (2013). Mechanical properties of graphene platelet-reinforced alumina ceramic composites. Ceram. Int. *39*, 6215–6221.

Magrini, T., Bouville, F., Lauria, A., Le Ferrand, H., Niebel, T.P., and Studart, A.R. (2019). Transparent and tough bulk composites inspired by nacre. Nat. Commun. *10*, 2794.

Mao, L.B., Gao, H.L., Yao, H.B., Liu, L., Colfen, H., Liu, G., Chen, S.M., Li, S.K., Yan, Y.X., Liu, Y.Y., et al. (2016). Synthetic nacre by predesigned matrix-directed mineralization. Science *354*, 107–110.

Morits, M., Verho, T., Sorvari, J., Liljeström, V., Kostiainen, M.A., Gröschel, A.H., and Ikkala, O. (2017). Toughness and fracture properties in nacre-mimetic clay/polymer nanocomposites. Adv. Funct. Mater. *27*, 1605378.

Munch, E., Launey, M.E., Alsem, D.H., Saiz, E., Tomsia, A.P., and Ritchie, R.O. (2008). Tough, bio-inspired hybrid materials. Science *322*, 1516–1520.

Naglieri, V., Gludovatz, B., Tomsia, A.P., and Ritchie, R.O. (2015). Developing strength and toughness in bio-inspired silicon carbide hybrid materials containing a compliant phase. Acta Mater. *98*, 141–151.

Nakagaito, A.N., Iwamoto, S., and Yano, H. (2005). Bacterial cellulose: the ultimate nano-scalar cellulose morphology for the production of high-strength composites. Appl. Phys. A *80*, 93–97.

Pan, X.F., Gao, H.L., Lu, Y., Wu, C.Y., Wu, Y.D., Wang, X.Y., Pan, Z.Q., Dong, L., Song, Y.H., Cong, H.P., et al. (2018). Transforming ground mica into high-performance biomimetic polymeric mica film. Nat. Commun. *9*, 2974.

Patterson, B.A., and Sodano, H.A. (2016). Enhanced interfacial strength and UV shielding of aramid fiber composites through ZnO nanoparticle sizing. ACS Appl. Mater. Interfaces *8*, 33963–33971.

Peng, J.S., and Cheng, Q.F. (2017). High-performance nanocomposites inspired by nature. Adv. Mater. *29*, 1902959.

Perez-Rodriguez, J.L., Wiewiora, A., Drapala, J., and Perez-Maqueda, L.A. (2006). The effect of sonication on dioctahedral and trioctahedral micas. Ultrason. Sonochem. *13*, 61–67.

Podsiadlo, P., Arruda, E.M., Kheng, E., Waas, A.M., Lee, J., Critchley, K., Qin, M., Chuang, E., Kaushik, A.K., Kim, H.S., et al. (2009). LBL assembled laminates with hierarchical organization from nano- to microscale: high-toughness nanomaterials and deformation imaging. ACS Nano *3*, 1564–1572.

Ritchie, R.O. (2011). The conflicts between strength and toughness. Nat. Mater. *10*, 817–822.

Shao, Y., Zhao, H.P., Feng, X.Q., and Gao, H.J. (2012). Discontinuous crack-bridging model for fracture toughness analysis of nacre. J. Mech. Phys. Sol. *60*, 1400–1419.

Song, J.W., Chen, C.J., Zhu, S.Z., Zhu, M.W., Dai, J.Q., Ray, U., Li, Y.J., Kuang, Y.D., Li, Y.F., and Quispe, N. (2018). Processing bulk natural wood into a high-performance structural material. Nature *554*, 224–228.

Wegst, U.G.K., Bai, H., Saiz, E., Tomsia, A.P., and Ritchie, R.O. (2015). Bioinspired structural materials. Nat. Mater. *14*, 23–36.

Xu, L.Z., Zhao, X.L., Xu, C.L., and Kotov, N.A. (2018). Biomimetic nanocomposites: water-rich biomimetic composites with abiotic self-organizing nanofiber network. Adv. Mater. *30*, 1870007.

Yang, B., Wang, L., Zhang, M.Y., Luo, J.J., and Ding, X.Y. (2019a). Timesaving, high-efficiency approaches to fabricate aramid nanofibers. ACS Nano *13*, 7886–7897.

Yang, B., Wang, L., Zhang, M.Y., Luo, J.J., Lu, Z.Q., and Ding, X.Y. (2020). Fabrication, applications, and prospects of aramid nanofiber. Adv. Funct. Mater. *30*, 2000186.

Yang, K., Wu, S.J., Guan, J., Shao, Z.Z., and Ritchie, R.O. (2017). Enhancing the mechanical toughness of epoxy-resin composites using natural silk reinforcements. Sci. Rep. *7*, 11939.

Yang, M., Cao, K.Q., Yeom, B., Thouless, M.D., Waas, A., Arruda, E.M., and Kotov, N.A. (2015). Aramid nanofiber-reinforced transparent nanocomposites. J. Compos. Mater. *49*, 1873–1879.

Yang, Y., Li, X.J., Chu, M., Sun, H.F., Jin, J., Yu, K.H., Wang, Q.M., Zhou, Q.F., and Chen, Y. (2019b). Electrically assisted 3D printing of nacre-inspired structures with self-sensing capability. Sci. Adv. *5*, eaau9490.

Yao, H.M., Dao, M., Imholt, T., Huang, J.M., Wheeler, K., Bonilla, A., Suresh, S., and Ortiz, C. (2010). Protection mechanisms of the iron-plated armor of a deep-sea hydrothermal vent gastropod. Proc. Natl. Acad. Sci. U S A *107*, 987–992.

Yin, Z., Hannard, F., and Barthelat, F. (2019). Impact-resistant nacre-like transparent materials. Science *364*, 1260–1263.

Yu, Z.L., Yang, N., Zhou, L.C., Ma, Z.Y., Zhu, Y.B., Lug, Y.Y., Qin, B., Xing, W.Y., Ma, T., Li, S.C., et al. (2018). Bioinspired polymeric woods. Sci. Adv. *4*, eaat7223.

Zhao, H.W., and Guo, L. (2017). Nacre-inspired structural composites: performance-enhancement strategy and perspective. Adv. Mater. *29*, 1702903.

Zhao, H.W., Yue, Y.H., Guo, L., Wu, J.T., Zhang, Y.W., Li, X.D., Mao, S.C., and Han, X.D. (2016). Cloning nacre's 3D interlocking skeleton in engineering composites to achieve exceptional mechanical properties. Adv. Mater. *28*, 5099–5105.

Zhu, H.L., Zhu, S.Z., Jia, Z., Parvinian, S., Li, Y.Y., Vaaland, O., Hu, L.B., and Li, T. (2015). Anomalous scaling law of strength and toughness of cellulose nanopaper. Proc. Natl. Acad. Sci. U S A *112*, 8971–8976.

iScience, Volume *24*

Supplemental Information

Nacreous aramid-mica bulk materials with excellent mechanical properties and environmental stability

Xiao-Feng Pan, Huai-Ling Gao, Kai-Jin Wu, Si-Ming Chen, Tao He, Yang Lu, Yong Ni, and Shu-Hong Yu

SUPPLEMENTAL INFORMATION

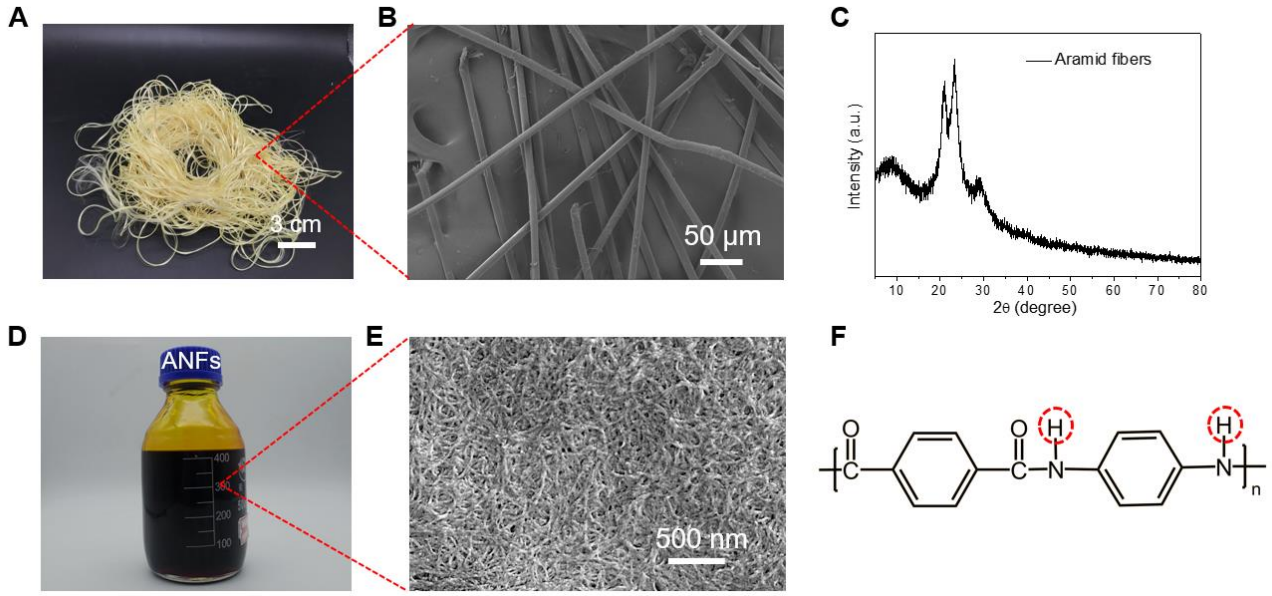

Figure S1. Characterization of aramid fibers, Related to Figure 1. (**A**) Photograph of aramid macrofibers. (**B**) SEM image showing the morphology of aramid macrofibers. The diameter of aramid macrofibers is ~12 μm. (**C**) XRD analysis of aramid macrofibers. (**D**) Photograph of 1 wt.% aramid nanofibers (ANFs) in dimethyl sulfoxide (DMSO) solution. (**E**) SEM image shows the morphology of ANFs, indicating that ANFs were successfully fabricated. (**F**) The molecular structure of ANFs in DMSO solution (Figure S1D), whose H atoms were captured by KOH in DMSO solution.

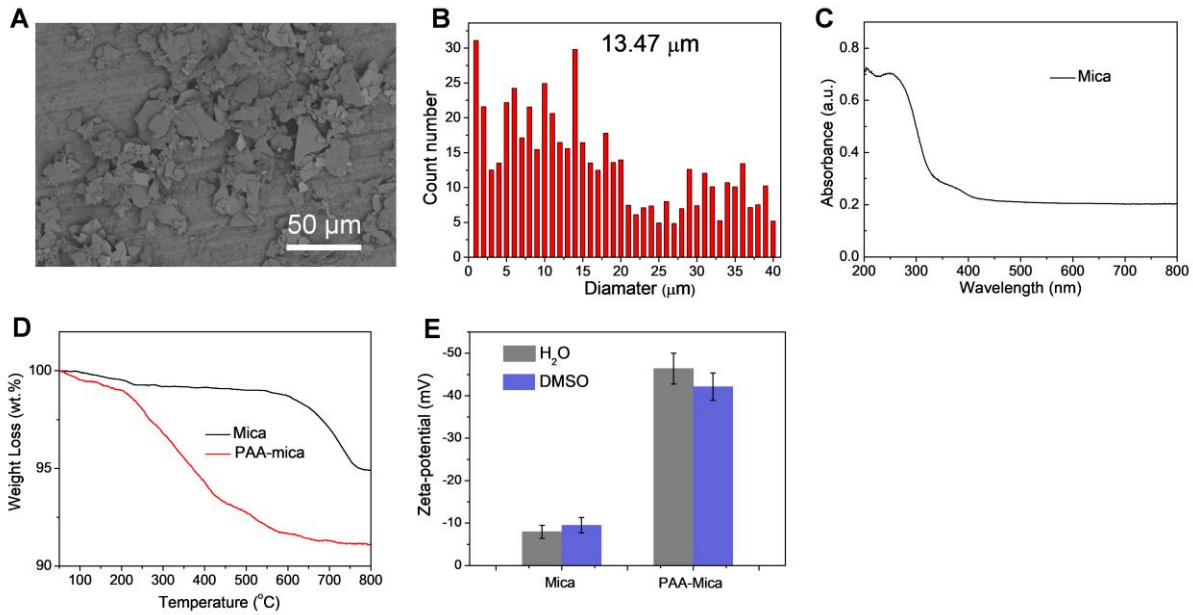

Figure S2. Characterization of mica microplatelets, Related to Figure 1. (**A-B**) SEM image and the statistical lateral size (13.47 μm) of mica microplatelets, which was determined by Nano Measurement Software. (**C**) UV-vis absorbance spectrum of mica microplatelets. (**D**) TGA curves of mica microplatelets and PAA modified mica microplatelets (PAA-mica). The content of PAA on the surface of mica microplatelets was measured to be ~4 wt.% by TGA. (**E**) Zeta potential values of the mica microplatelets and PAA-mica dispersed in deionized water (DIW) and DMSO, respectively. The zeta-potential of mica microplatelets dispersed in DIW is about -7.93 mV. The zeta-potential of PAA-mica dispersed in DIW is about -46.40 mV due to the anionic PAA modification (Alkilany et al., 2009). In addition, the larger negative surface charge of PAA-mica relative to that of mica in DMSO dispersion indicates that PAA molecules are adsorbed stably on the surface of mica in DMSO solution. The pH of the above mica dispersions is about 7. In addition, it has been confirmed that montmorillonite (MTM) and PAA have a good interface interaction via forming hydrogen bonds, which are formed between the Si-OH group of MTM and the COOH group of PAA (Kim et al., 2014), and the surface of mica has the same functional groups (Si-OH group) as that of MTM (Jia and Song, 2014). Thus, we can conclude that the interfacial interaction between mica and PAA is also hydrogen bonding.

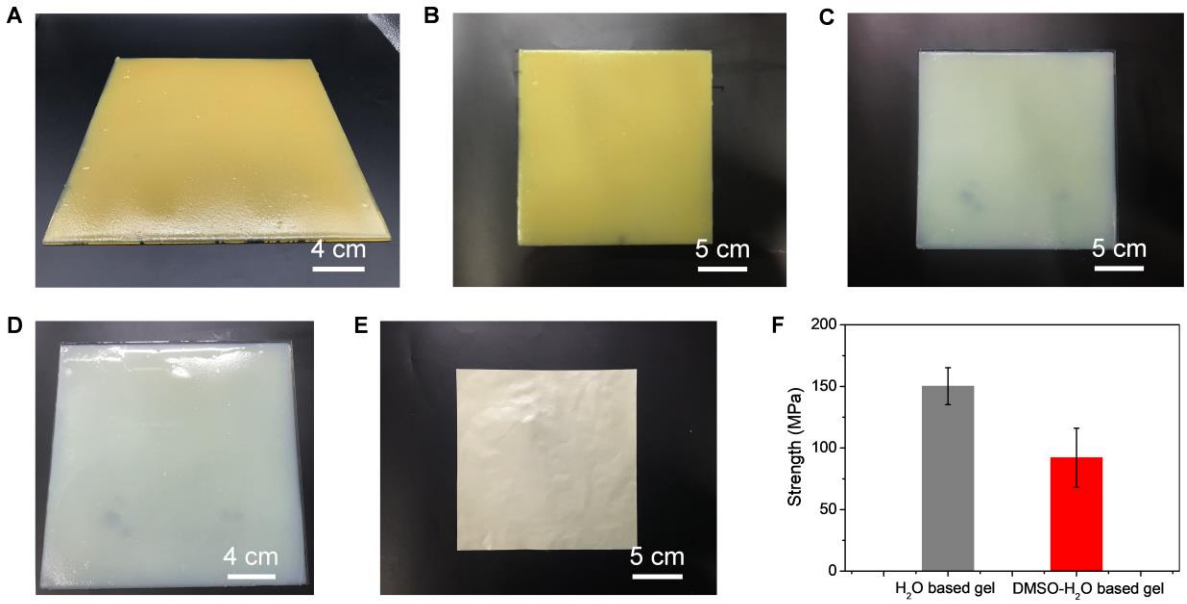

Figure S3. Process of the as-fabricated nacre-mimetic films, Related to Figure 1. (**A-B**) Photographs of ANFs-Mica-DMSO-H_2O gel obtained via a spray-assisted gelation method. (**C-D**) Photographs of ANFs-Mica-H_2O gel after exchanging DMSO with DIW. (**E**) Photograph of ANFs-Mica film obtained via drying the ANFs-Mica-H_2O gel. Following these procedures, large-sized nacreous ANFs-Mica films with no planar dimensional restriction could be efficiently prepared. (**F**) Tensile strength of the pure ANFs film from H_2O based gel, and pure ANFs film from DMSO-H_2O based gel. In the process of solvent exchange from DMSO to water, the molecular structure of ANFs was restored by protonation (Yang et al., 2019), leading to a great mechanical improvement of the resultant ANFs film.

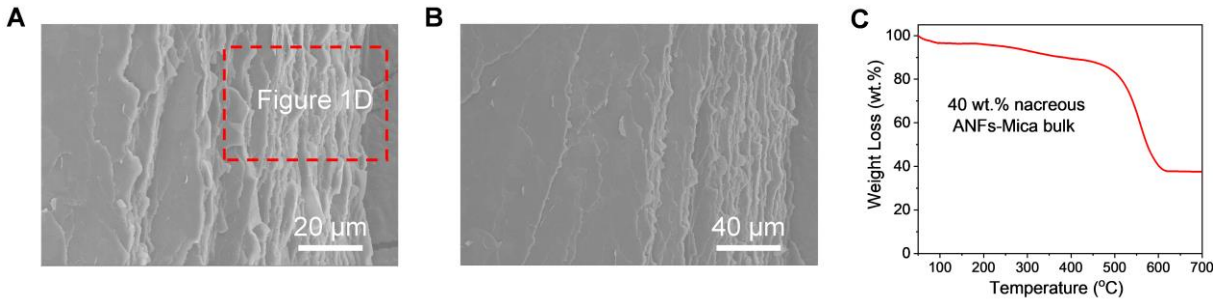

Figure S4. The fracture surface of 40 wt.% nacreous ANFs-Mica bulk, Related to Figure 1. (**A-B**) Low-magnification cross sectional SEM images of the 40 wt.% nacreous ANFs-Mica bulk, showing nacreous layered structure at large length scale. (**C**) TGA curve of the 40. wt% nacreous ANFs-Mica bulk materials. Its microplatelets content is about 38 wt.%, which is close to experimental data of 40. wt%.

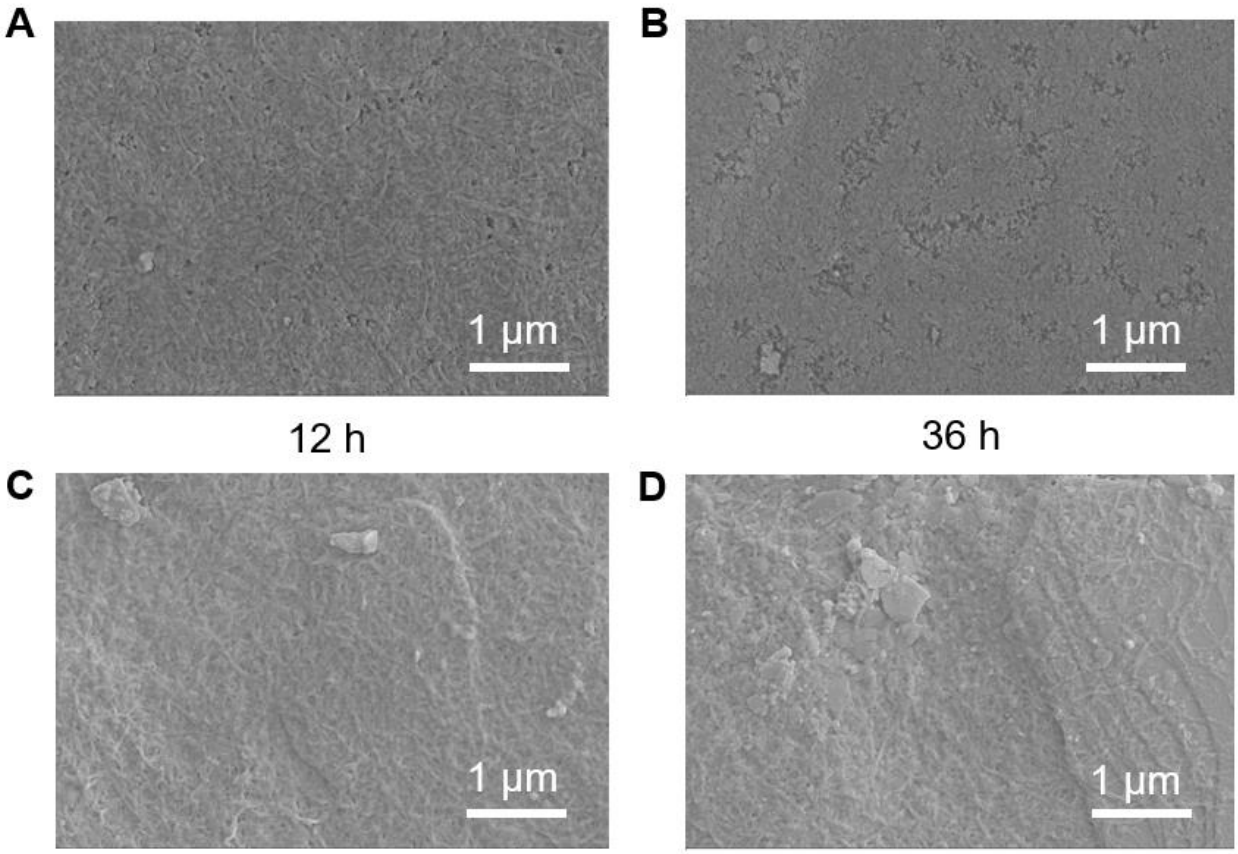

Figure S5. Surface morphology of different bulk materials after UV radiation, Related to Figure 1. Surface SEM images of (**A-B**) the pure ANFs bulk and (**C-D**) 40 wt.% nacreous ANFs-Mica bulk treated with UV radiation for 12 h and 36 h, respectively. Surfaces of the pure ANFs bulk show many cracks and etching phenomenon. In contrast, Surfaces of the nacreous ANFs-Mica bulk do not display the phenomenon.

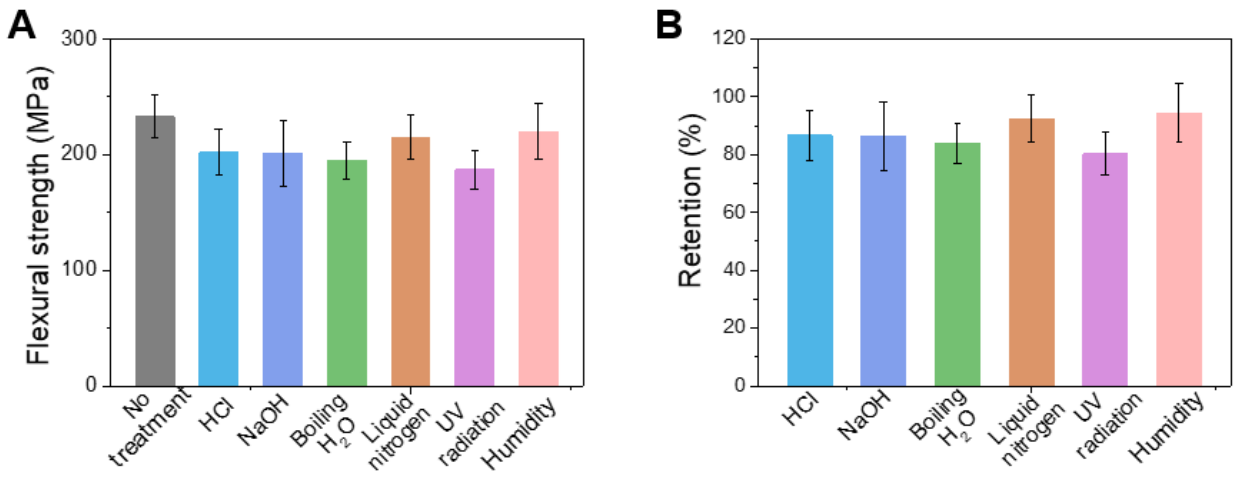

Figure S6. Mechanical properties of the pure ANFs bulk materials subjected to some adverse environments, Related to Figure 1. (**A-B**) Flexural strength and its retention of the pure ANFs bulk materials, respectively, after treatment by 1 mol L^{-1} HCl solution (24 h), 1 mol L^{-1} NaOH solution (24 h), boiling water (24 h), liquid nitrogen (24 h), UV radiation (6 days) and 80% relative humidity (RH) (24 h). Note that, the RH environment was achieved via saturated potassium bromide solution at 25 ^{o}C.

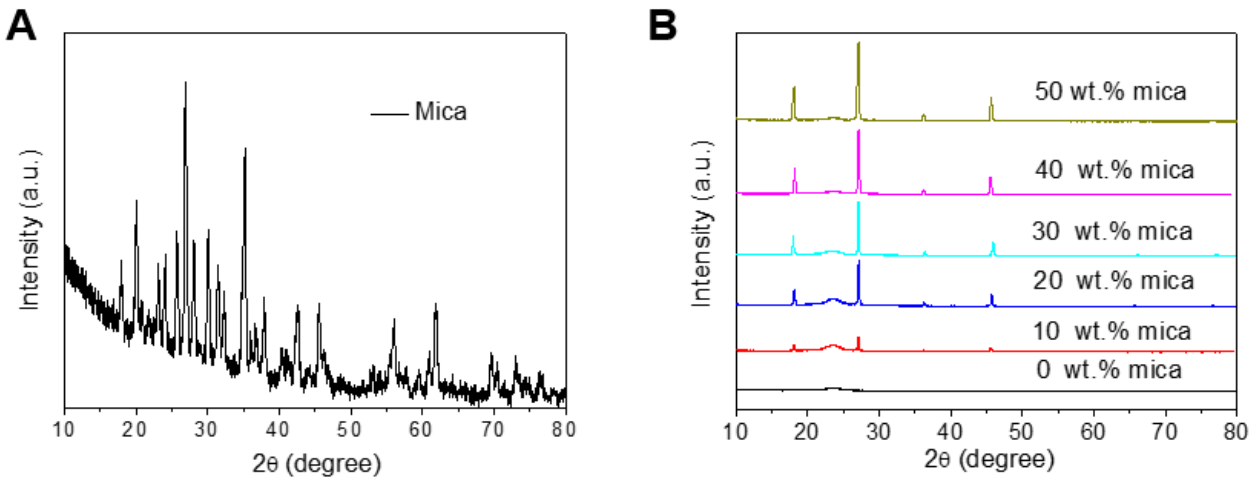

Figure S7 XRD characterization of mica and ANFs-Mica films, Related to Figure 2. (**A**) XRD pattern of mica microplatelets. (**B**) XRD analyses of ANFs-Mica films with different mica content. XRD patterns of these nacreous ANFs-Mica films with different mica loading can match those of pure mica and ANFs. Furthermore, the observed diffraction peaks of ANFs are similar to those of aramid macrofibers, indicating the reservation of the crystalline polyparaphenylene terephthalamide structures in the nanoscale domains (Zhu et al., 2015).

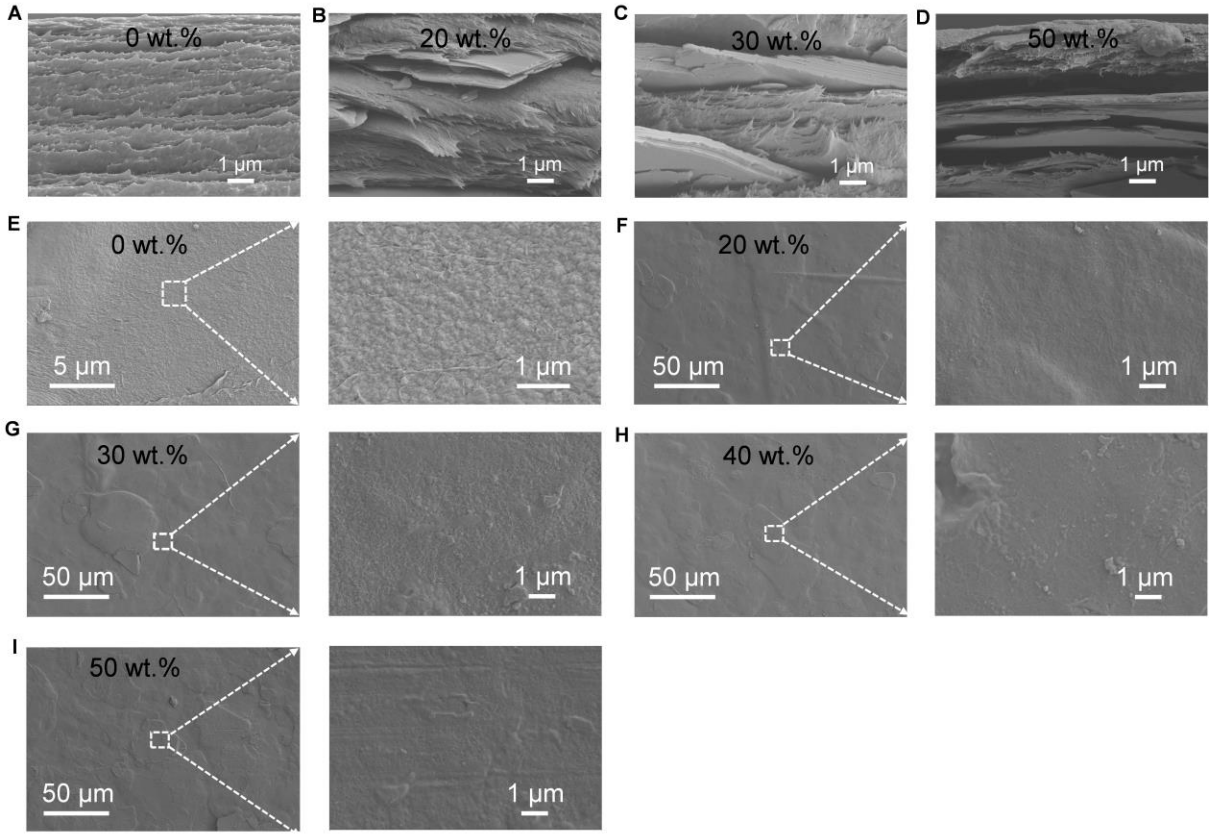

Figure S8 Microstructural observation of the nacreous ANFs-Mica films with different mica content, Related to Figure 2. (**A-D**) SEM images show cross-section of the nacreous ANFs-Mica films with different mica content, displaying obvious "bricks-and-mortar" structure. (**E-I**) SEM images with different magnifications show surfaces of the nacreous ANFs-Mica films with different mica content, indicating that mica microplatelets and ANFs are tightly bound together, and mica microplatelets are uniformly lying flat in parallel to the film surface.

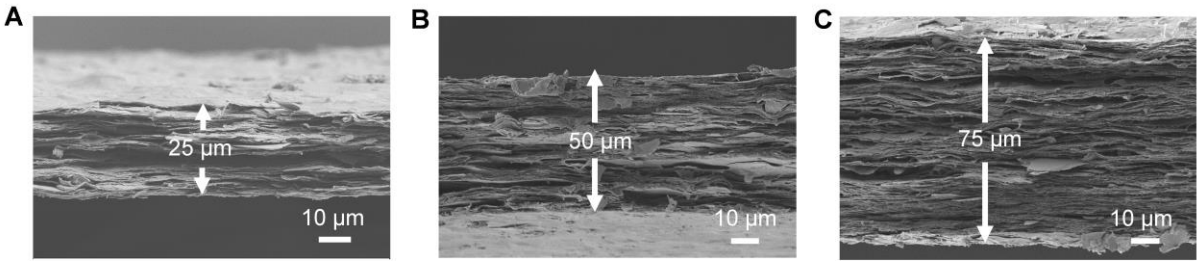

Figure S9 Nacreous ANFs-Mica films (40. wt%) with different thickness, Related to Figure 2. (**A-C**) Cross-sectional SEM images of the nacreous ANFs-Mica films with thickness of about 25 μm, 50 μm and 75 μm, respectively.

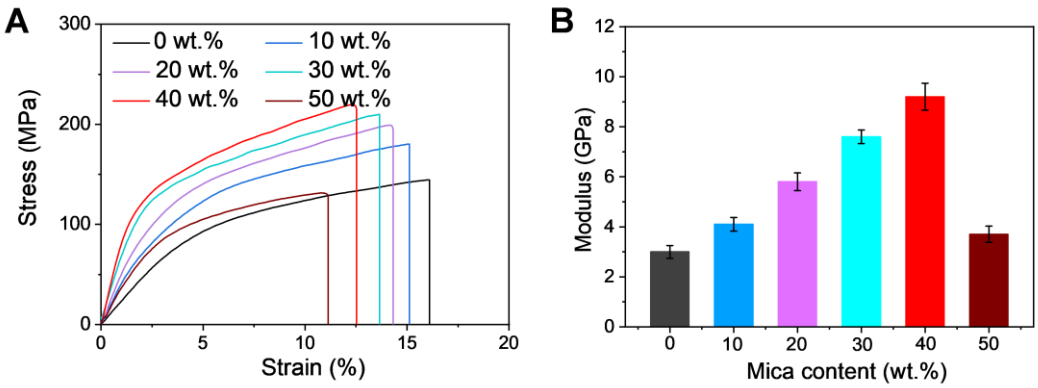

Figure S10 Mechanical properties of nacreous ANFs-Mica films with different mica content, Related to Figure 2. (**A-B**) Stress-strain curves and modulus of the nacreous ANFs-Mica films containing different mica content. Error bars manifest standard s.d. of at least six measurements.

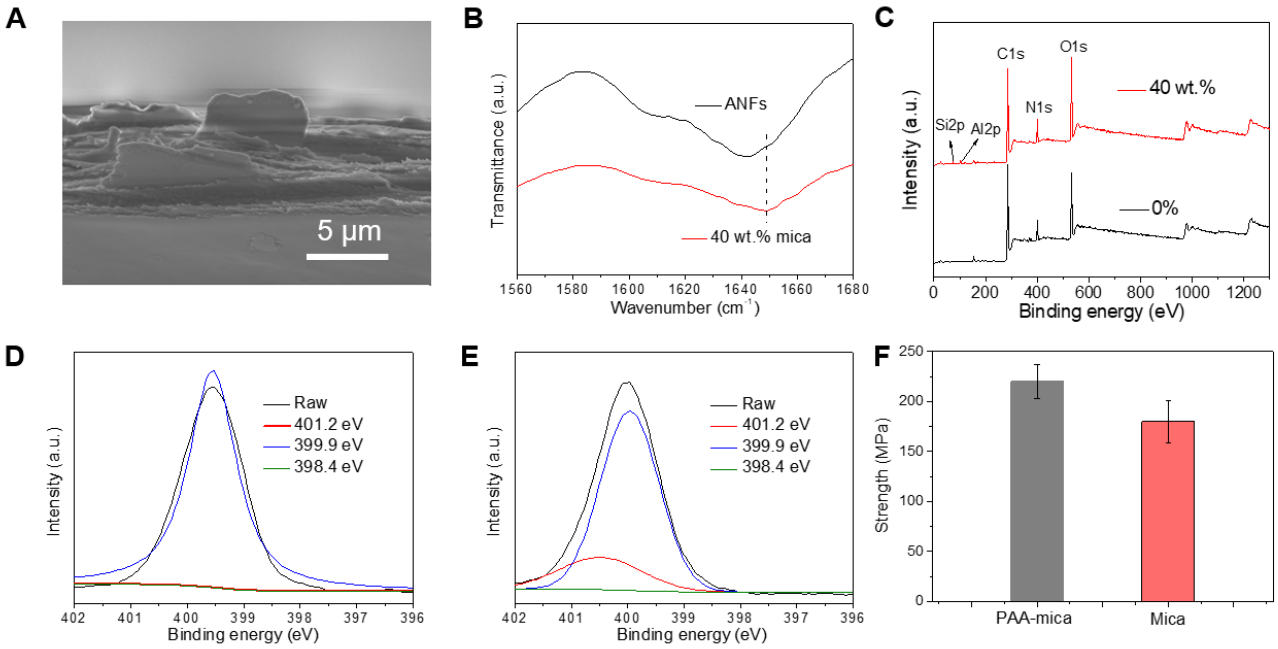

Figure S11 Interface characterization of the ANFs-Mica film containing 40 wt.% mica, Related to Figures 2 and 3. (A) SEM image shows fracture surface of the 40 wt.% ANFs-Mica film after tensile test, revealing that many mica microplatelets are obviously pulled out. (**B**) FT-IR spectra of the ANFs and 40 wt.% ANFs-Mica films. The blue shift from ~1640 cm^{-1} to ~1650 cm^{-1} (the CO group from ANFs) was observed in the FT-IR spectrum of 40 wt.% ANFs-Mica film. In addition, Blue shift of the peak of hydrogen bond (the CO group from ANFs) in FT-IR spectra have been found in many recent ANFs based composites, including ANFs/PVA, (Guan et al., 2017) ANFs/PAA, (Yang et al., 2015) ANFs/MWCNT, (Zhu et al., 2015) ANFs/MTM, (Si et al., 2020) *etc*. These results suggest the hydrogen bonding is formed between the CO group of ANFs and the COOH group of PAA-mica. (**C**) Survey XPS patterns of the ANFs and 40 wt.% ANFs-Mica films. (**D-E**) N1s survey analyses of the ANFs and 40 wt.% ANFs-Mica films. For pure ANFs film, the N1s peak is centered at ~399.5 eV, which can be deconvoluted into two components. In addition, the N1s peak from XPS spectrum of 40 wt.% ANFs-Mica film was found at an higher (~400.0 eV) peak, which can be decomposed into three components. It should mainly ascribe to the formation of hydrogen bonding between NH group from ANFs and the COOH group on the surface of the PAA-mica (Ma et al., 2019; Zhu et al., 2015). (**F**) Comparison of the tensile strength of 40 wt.% ANFs-Mica films assembled from mica and PAA-mica. Moreover, the nacreous ANFs-Mica film (40 wt.%) assembled from ANFs and PAA-modified mica was tested to have stronger mechanical strength than that from ANFs and mica without PAA modification. This result indicates that there was a strong interfacial interaction between ANFs and PAA-mica via forming hydrogen bonds.

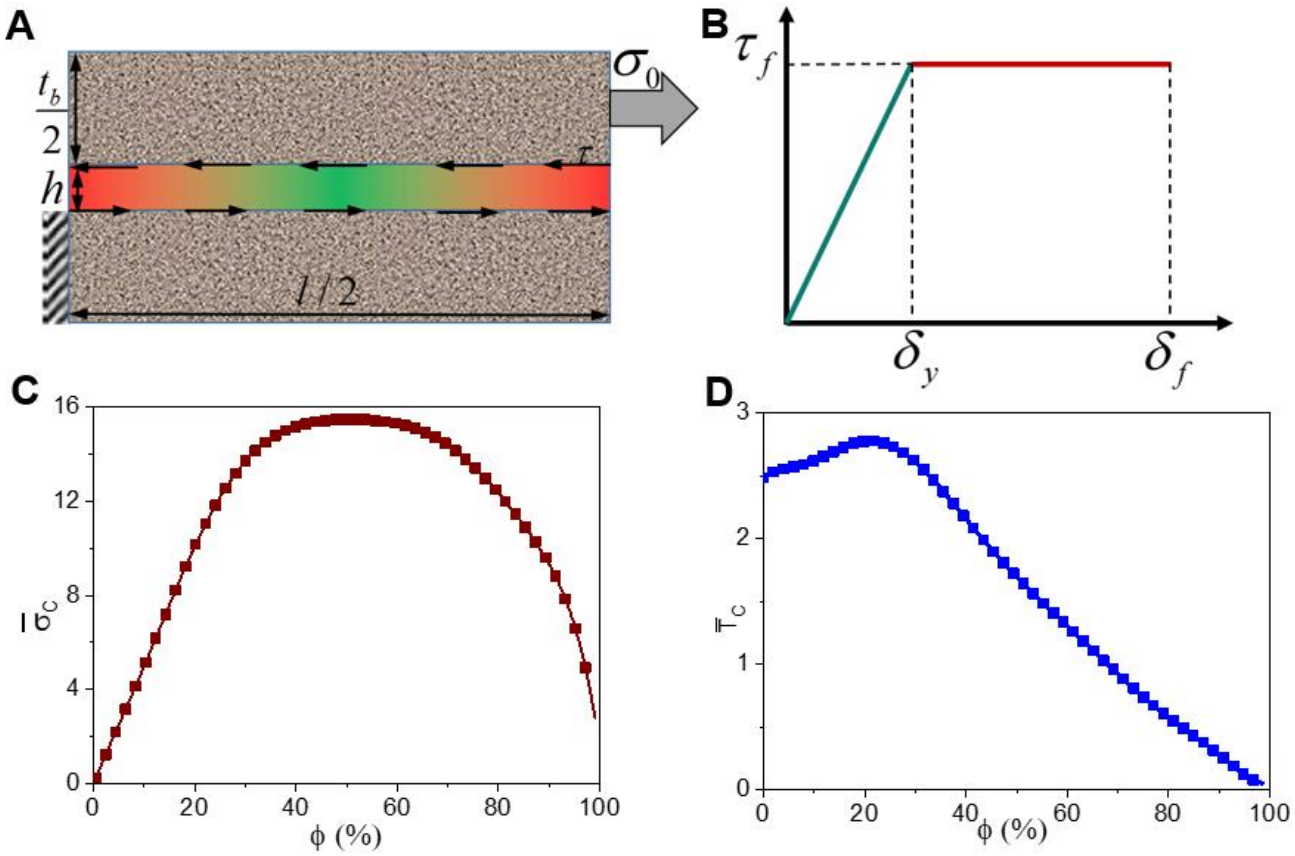

Figure S12 The effect of platelet volume fraction on the mechanical properties of nacreous ANFs-Mica film, Related to Figure 2. (**A-B**) Schematic view of a unit cell and an elastic-perfectly plastic shear deformation model. (**C-D**) The effects of volume fractions of platelets ϕ on the (**C**) normalized strength $\bar{\sigma}_c$ and (**D**) normalized toughness. The result reveal that there exist optimum volume fractions of mica platelets that maximize the strength and toughness of the nacreous ANFs-Mica composite, which is consistent with the experimental investigations. The underlying physical mechanism can be explained by that the capacity of transferring shear loads in the ANFs crosslinked interface significantly depends on the density of interfacial hydrogen bonds, i.e., the volume fractions of interlayer crosslink. It is worth mentioning that different values of optimum volume fractions depend on the material properties and geometry parameters, and the detailed analyses can be found in the Transparent Method section.

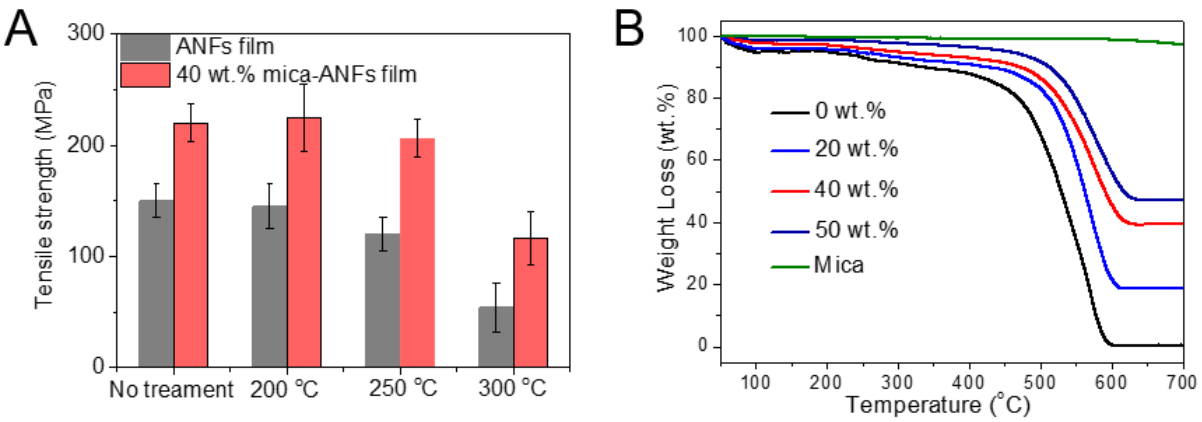

Figure S13 Mechanical properties of these films after thermal treatment, Related to Figure 2. (**A**) Tensile strength of the 40 wt.% nacreous ANFs-Mica film and pure ANFs film after 200 °C, 250 °C and 300 °C treatment for 6 h, respectively. (**B**) TGA curves of mica microplatelets and the nacreous ANFs-Mica films with different mica contents. Error bars manifest standard s.d. of at least six measurements.

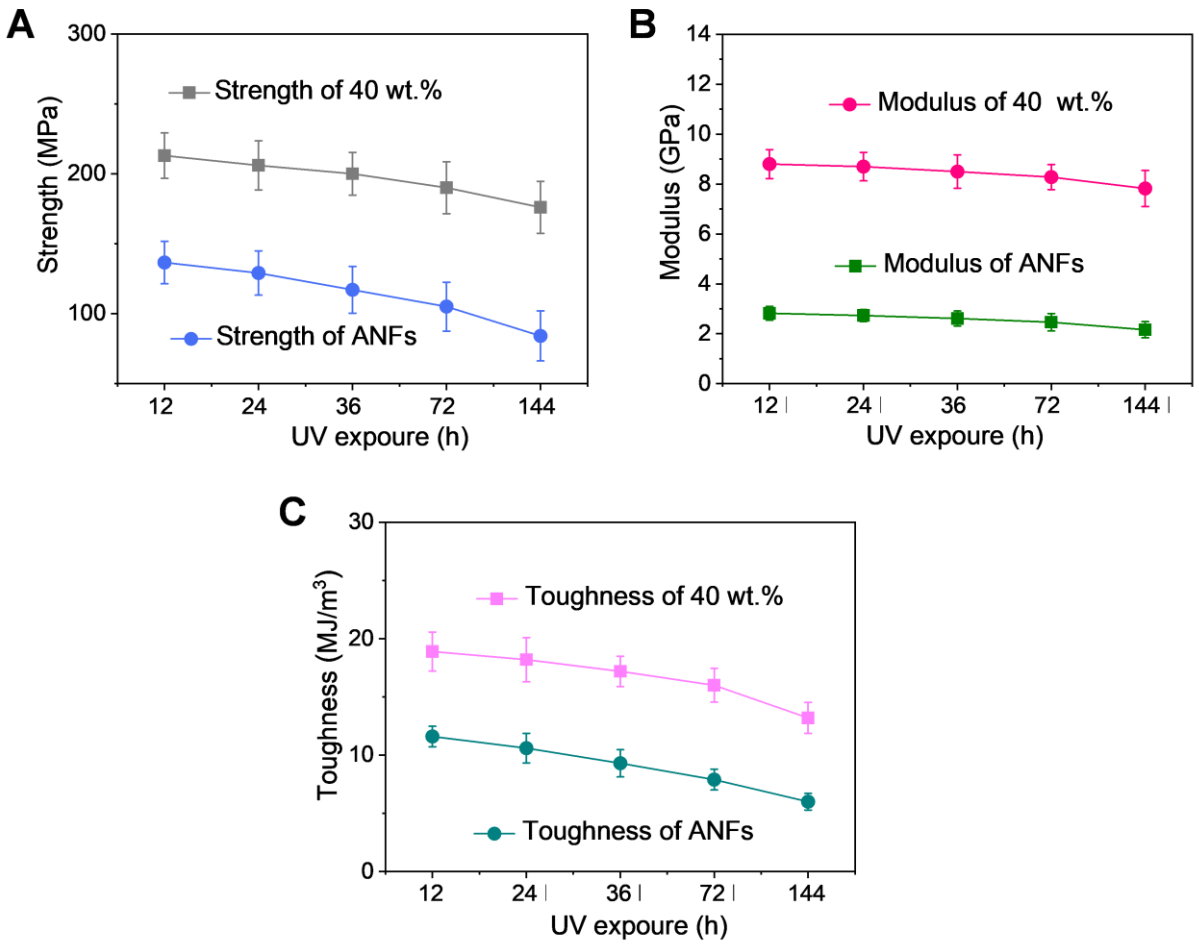

Figure S14 Mechanical properties of these films after UV radiation treatment, Related to Figure 2. (**A-C**) Comparison of tensile strength, Young's modulus and toughness of the 40 wt.% ANFs-Mica film and pure ANFs film after UV radiation treatment for different times, respectively. Error bars manifest standard s.d. of at least six measurements.

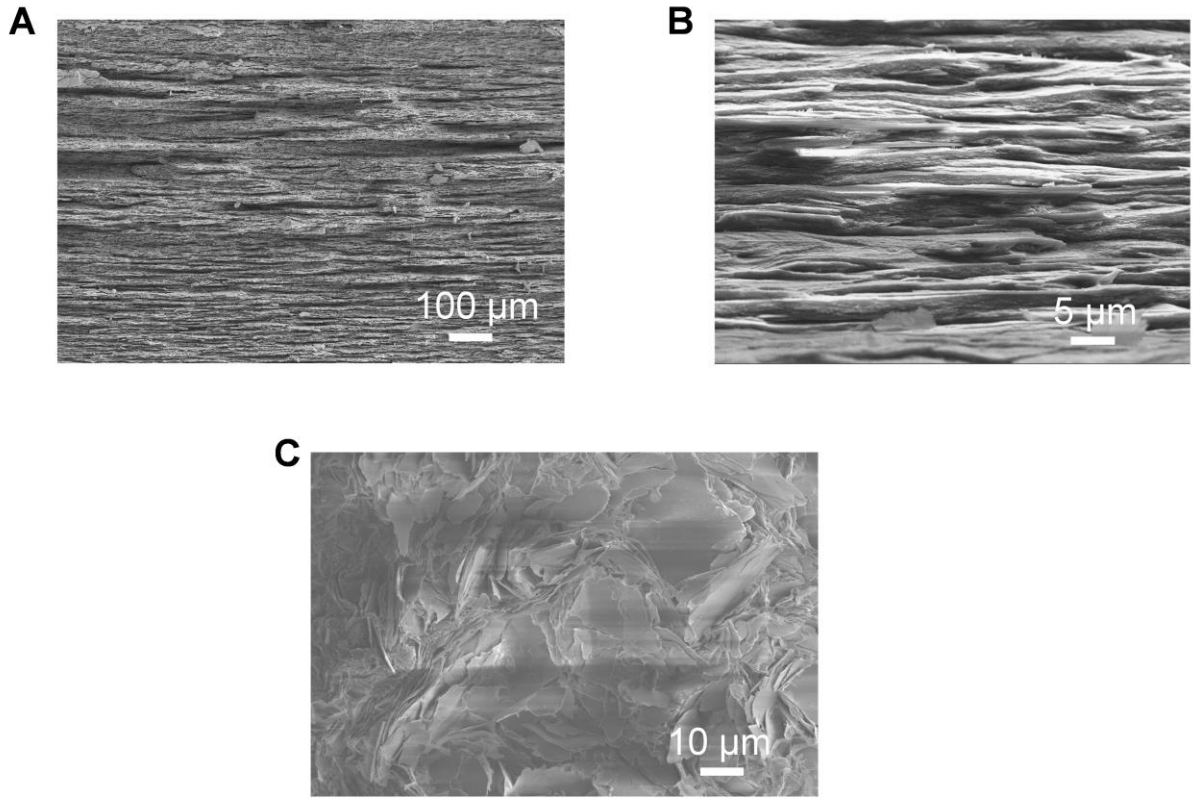

Figure S15 Structural characterizations of the as-prepared the 40 wt.% ANFs-Mica bulk, Related to Figure 3. (**A**) Low-magnification cross sectional SEM image of the nacreous ANFs-Mica bulk (40 wt.%). (**B**) High-magnification cross-sectional SEM image of the 40 wt.% nacreous ANFs-Mica bulk. **(C)** SEM image of the 40 wt.% disordered ANFs-Mica bulk.

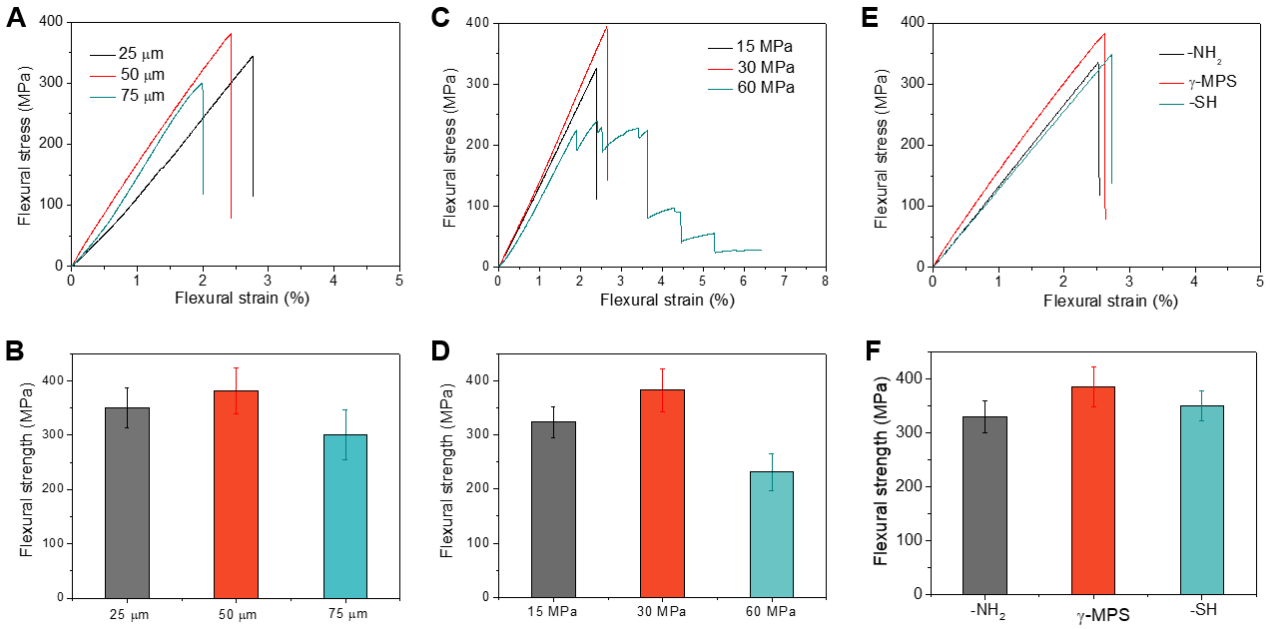

Figure S16 Comparison of flexural strength of these 40 wt.% nacreous ANFs-Mica bulks fabricated under different conditions, Related to Figure 3. (**A-F**) Flexural stress-strain curves and strength of the nacreous bulk materials as a function of the thickness of the utilized 40 wt.% nacreous ANFs-Mica films (**A-B**), the pressures in the hot-pressing process (**C-D**), and the type of utilized coupling reagents (**E-F**). In our experiment, nacreous ANFs-Mica films with ~50 μm thickness were chose, the applied pressure was 30 MPa, and coupling agent of γ-MPS was used. When the film thickness increased to ~75 μm, the flexural strength of the as-fabricated nacreous bulk materials decreased. It can be ascribed to the decreased number of the interfaces between adjacent films at an equal thickness of the bulk materials. For the nacreous ANFs-Mica bulk, the mechanical properties depend on both the interfacial defects and the capacity of load transfer in the interfaces among the laminated films. The interfacial defects played the main role when the laminated films were very thin (25 μm), because defects appeared easily due to manual operation. The interfacial interaction played the main role when the thickness of the laminated films increased. We have certified that the interfacial modification with γ-MPS greatly enhanced the mechanical properties of the ultimate materials compared with the no modification one (Figures 3B-3E). Thus, decreasing the number of the interfaces (using thicker films) would lower the mechanical properties of the ultimate bulk materials with equal thickness (Gao et al., 2017). Higher pressure causes lower ultimate flexural strength of obtained nacreous bulk material, which could be attributed to the damaged nacreous ANFs-Mica films under the higher applied pressure. As γ-MPS is a coupling reagent of organic functional groups, secondary nacreous ANFs-Mica films were further grafted with γ-MPS to allow the monomer of epoxy resin to react with it during the successive hot-pressing step. Error bars manifest standard s.d. of at least six measurements.

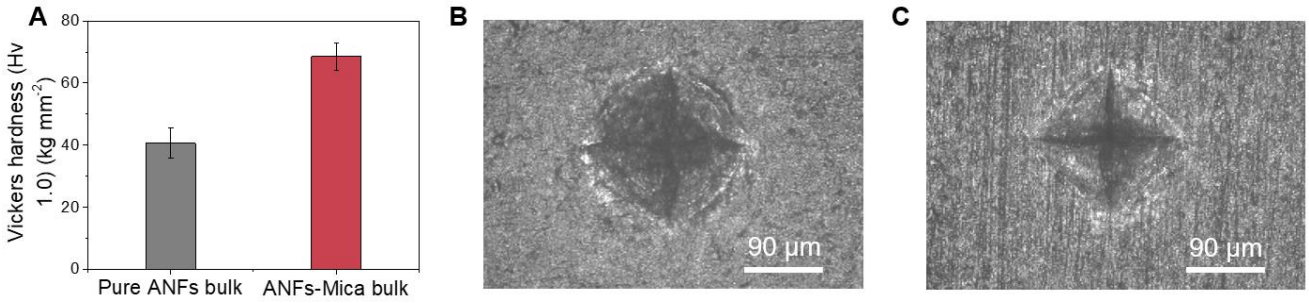

Figure S17 Vickers hardness of the different bulk materials, Related to Figure 3. (**A**) Vickers hardness of the 40 wt.% nacreous ANFs-Mica bulk and the pure ANFs bulk. **(B-C)** SEM images show the indentation on surface of the pure ANFs bulk (**B**) and the 40 wt.% nacreous ANFs-Mica bulk (**C**), respectively. Error bars manifest standard s.d. of at least six measurements.

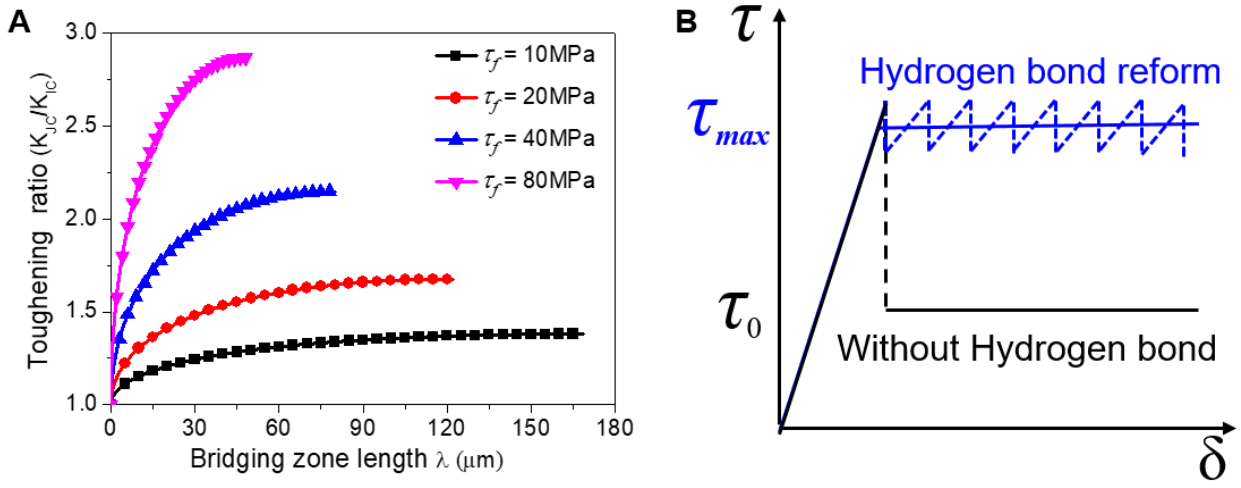

Figure S18 Theoretical analysis of toughening mechanisms of the nacreous ANFs-Mica bulk, Related to Figure 3. (**A**) The influence of the interfacial strength τ_{max} on the toughening ratio (K_{JC}/K_{IC}) under different bridging length λ during the crack propagation. (**B**) The schematic of cohesive model for the interfacial shear stress with or without hydrogen bonds. The effects of interfacial properties on the fracture toughness of the nacreous ANFs-Mica bulk were analysed through crack-bridging model (Budiansky and Amazigo, 1989; Shao et al., 2012). The schematic of the crack-bridging model for the nacreous ANFs-Mica bulk with "brick-and-mortar" microstructure is shown in Figure 3F. Firstly, we analysed the interfacial hydrogen bond network at the molecular scale, as shown in the Figure 3G. The hydrogen bonds are formed between NH and CO groups of adjacent ANFs chains. In addition, they are formed between the COOH group on the surface of the mica microplatelets modified with PAA and the NH and CO groups of ANFs, respectively. There exist repeated breaking and forming of interfacial hydrogen bonds during the pullout process of neighboring platelets, which dissipate a significant amount of energy. The cohesive shear strength of the ANFs crosslinked interface significantly depends on the density of interfacial hydrogen bonds (Chowdhury and Gillespie, 2018; Wu et al., 2018). Figure S18 shows that the toughening ratio increase with the increase of the size of crack-bridging zone before crack-bridging zone is saturated, which is in good agreement with the R-curve in Figure 3H. In the meanwhile, Figure S18A indicate that stronger interfacial strengths are beneficial for the improvement of the fracture toughness. Figure S18B shows that the shear strength τ_{max} of the interface with hydrogen bonds remains high constant value during the pullout process due to the reformation of hydrogen bonds network. The fracture toughness of nacreous ANFs-Mica bulk is larger than that of nacreous ANFs-Mica bulk without PAA modification, which is attributed to that the hydrogen bonds reforming improves the interfacial strength.

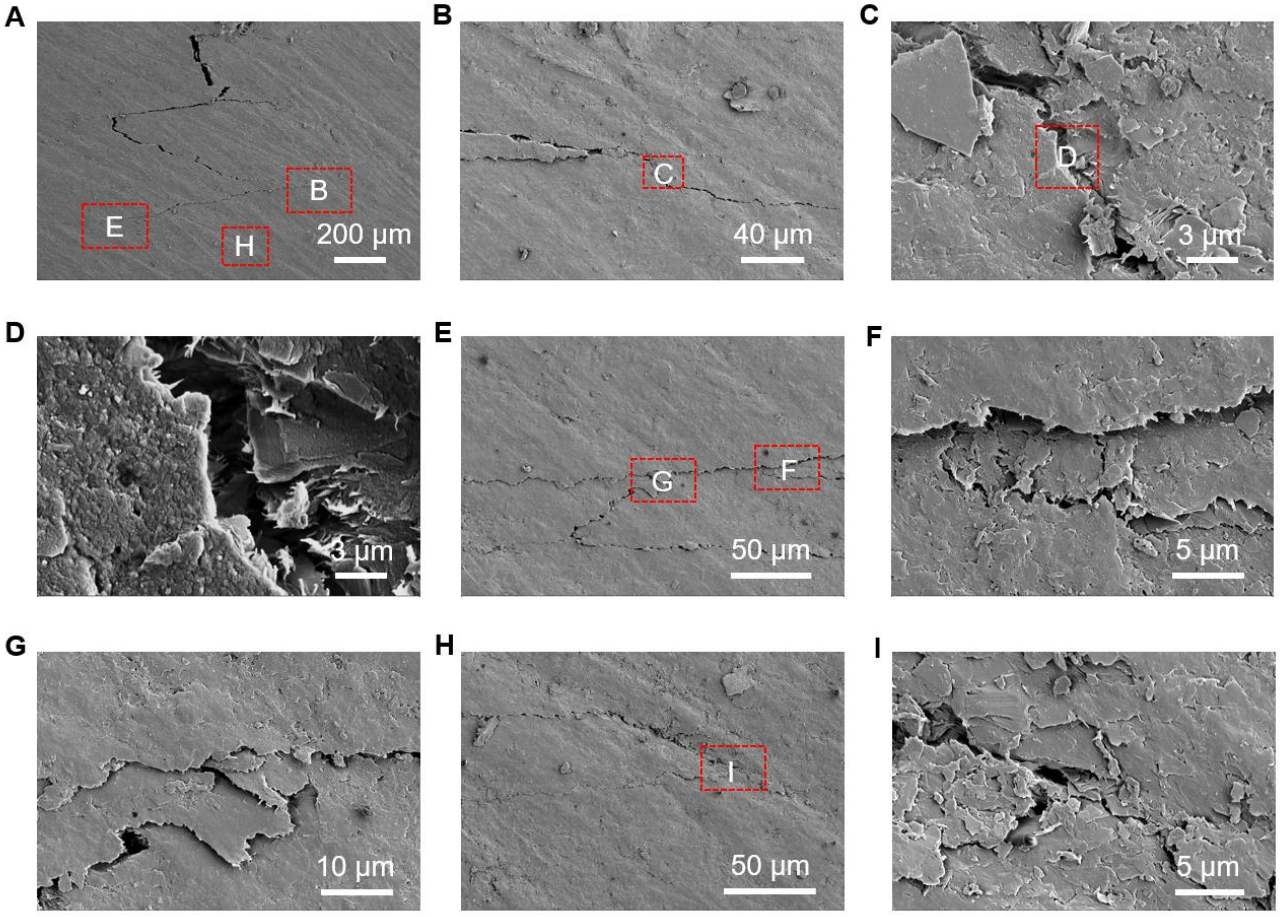

Figure S19 Structural analysis of toughening mechanisms of the nacreous ANFs-Mica bulk, Related to Figure 3. (**A**) A long-range crack extension path. (**B, E and H**) Crack deflection, crack branching and multiple cracking at the crack tip. (**C, D and I**) Microcrack deflection and (**F-G**) crack bridging toward deflection direction of the crack path.

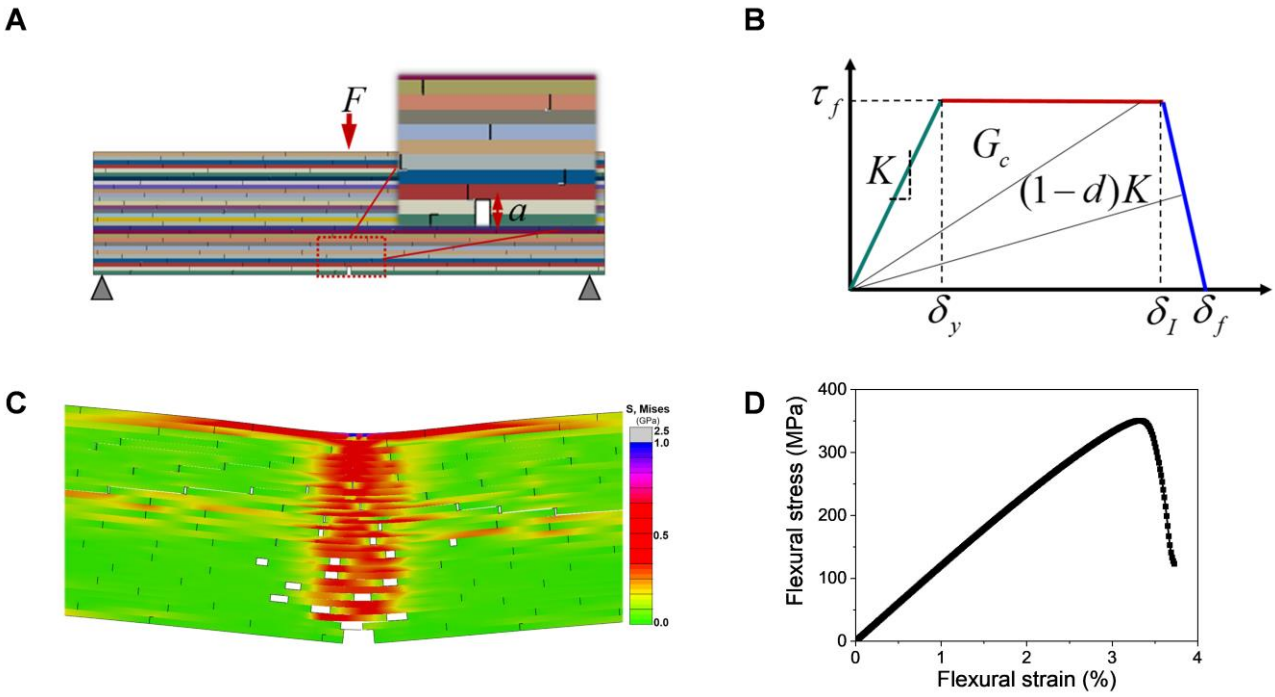

Figure S20 Finite element (FE) analysis of the nacreous hierarchical structure under three-point bending, Related to Figure 3. (**A**) The initial configuration of the 3D nacreous structure under three-point bending. (**B**) Typical post-damage-initiation response based on trapezoidal damage evolution of cohesive mode. (**C**) The Mises stress field distributions show the progressive interface failure included interlayer sliding, cracking bridging and crack deflection based on FEM simulation. (**D**) Plot of the flexural stress and flexural strain in three-point bending using Abaqus simulation. The simulated results show a torturous path include interlayer sliding, platelets' pull-out and crack deflection, and these simulated fracture features under crack propagation are consistent with those observed in experiments of the nacreous ANFs-Mica composite. The progressive interface failure in the nacreous structure toughens the composite with nacreous structure and resists its catastrophic failure. It is worth mentioning that the FE model using a cohesive zone model with the trapezoidal cohesive law indicates the important toughening effects of the tablet sliding accompanied by the reformation of hydrogen bonds, which generates nonlinear deformations over large volumes and significantly improves toughness (Yin et al., 2019). These predicted toughening behaviors of the nacreous hierarchical structure clearly illustrate the underlying mechanisms of the tough nacreous ANFs-Mica composite.

Table S1 Parameters used in the calculations, which are based on experiment data, Related to Figure 3.

l	t_b	E	Φ	K_{IC}	τ_{max} (with H-bonds)(Chowdhury and Gillespie, 2018)
13.47 μm	0.4 μm	20 GPa	0.25	3 MPa·m$^{1/2}$	200 MPa

Table S2 Mechanical properties of the nacreous ANFs-Mica bulk compared with natural, biomimetic, and engineering structural materials, Related to Figure 4. Numbers of the references are related to that in the charts of Figure 4.

Materials		Density (g cm^{-3})	Flexural strength (MPa)	Fracture Toughness K_{jc} (MPa $m^{1/2}$)	Specific strength (MPa/(Mg m^{-3}))	Specific toughness (MPa $m^{1/2}$/(Mg m^{-3}))	Reference	Number
Natural structural material	Nacre	2.58	171.7 (s.d. = 51.4)	5.9 (s.d. = 0.85)	66.54 (s.d. = 19.93)	2.28 (s.d. = 0.33)	(Gao et al., 2017)	1
	Wood	0.76	8.03 (s.d. = 2.11)	7 (s.d. = 2)	10.56 (s.d. = 2.78)	9.21 (s.d. = 1.97)	(Gao et al., 2017)	1
	Enamel	-	-	3 (s.d. = 0.5)	-	-	(Gao et al., 2017)	1
Biomimetic structural material	Al_2O_3/SiO_2	3.0	470 (s.d. = 42)	22 (s.d. = 3.6)	156.7 (s.d. = 14.1)	7.3 (s.d. = 1.2)	(Bouville et al., 2014)	2
	Al_2O_3/PMMA	3.0	210 (s.d. = 15)	30 (s.d. = 1.5)	70 (s.d. = 5)	10 (s.d. = 0.5)	(Munch et al., 2008)	3
	Al_2O_3/SiO_2	3.94	650 (s.d. = 30)	14 (s.d. = 2.4)	165 (s.d. = 7.6)	3.6 (s.d. = 0.61)	(Le Ferrand et al., 2015)	4
	Al_2O_3/PMMA	2.52	220	30	87	3.4	(Le Ferrand et al., 2015)	4
	Al_2O_3/Cu	3.96	300 (s.d. = 20)	11 (s.d. = 1.182)	76 (s.d. = 5.01)	2.8 (s.d. = 0.3)	(Le Ferrand et al., 2015)	4
	Al_2O_3/SCMC	1.85	300 (s.d. = 20)	-	162 (s.d. = 10.8)	-	(Zhao et al., 2016)	5
	HA/SA	1.8	267 (s.d. = 24.2)	8.55 (s.d. = 1.19)	145.9 (s.d. = 13.4)	4.75 (s.d. = 0.66)	(Gao et al., 2017)	1
	MTM/PVA	1.8	220	3.4	122.2	1.9	(Morits et al., 2017)	6
	Synthesis nacre	2.18	63 (s.d. = 10.9)	2.34 (s.d. = 0.6)	29 (s.d. = 5)	1.075 (s.d. = 0.275)	(Mao et al., 2016)	7
	Al_2O_3/epoxy	2.18	185 (s.d. = 10.9)	2.6 (s.d. = 0.2)	85 (s.d. = 5)	1.2 (s.d. = 0.1)	(Libanori et al., 2013)	8
	Al_2O_3/C	3.95	523 (s.d. = 30)	4.49 (s.d. = 0.33)	132 (s.d. = 7.9)	1.14 (s.d. = 0.08)	(Liu et al., 2013)	9
	Al_2O_3/CNT	3.544	403.7 (s.d. = 18)	4.62 (s.d. = 0.2)	113.91 (s.d. = 5.08)	1.304 (s.d. =0.056)	(Estili et al., 2012)	10
	Al_2O_3/TiO_2	2.96	370 (s.d. = 30)	6.6 (s.d. = 1)	125 (s.d. = 10.1)	2.23 (s.d. = 0.34)	(Grossman et al., 2017)	11
	Densified wood	1.3	336.8 (s.d. = 11.3)	-	258.5 (s.d. = 8.7)		(Song et al., 2018)	12
	HA–SA twisted plywood	1.68	257 (s.d. = 15.5)	9.3 (s.d. = 1)	153.4 (s.d. = 9.2)	5.55 (s.d. = 0.59)	(Chen et al., 2018)	13
	Nacre-like alumina		336 (s.d. = 168)	5 (s.d. = 1.2)			(Wat et al., 2019)	14
	Ap-SFRP	1.26	398.6 (s.d. = 16.4)	42.3 (s.d. = 1.5)	316.3 (s.d. = 13)	33.6 (s.d. = 1.19)	(Yang et al., 2017)	15
	MFC-based composites	1.1	425				(Nakagaito et al., 2005)	16

	cellulose nanofiber plate	1.35	324		240		(Guan et al., 2020b)	17
	bioinspired structural material	1.7	281	6.7	165	3.9	(Guan et al., 2020a)	18
	SiC/PMMA	2.54	165 (s.d. = 20)	5.5 (s.d. = 0.3)	65 (s.d. = 7.9)	2.16 (s.d. = 0.12)	(Naglieri et al., 2015)	19
Engineering structural material	Al	2.7	8.9 (s.d. = 2.0)	21.1 (s.d. = 7.0)	3.3 (s.d. = 0.7)	7.8 (s.d. = 2.6)	(Gao et al., 2017)	1
	Al-alloys	2.8	212.8 (s.d. = 151.2)	30.52 (s.d. = 11.48)	76 (s.d. = 54)	10.9 (s.d. = 4.1)	(Bouville et al., 2014)	2
	Al_2O_3	3.96	395.8 (s.d. = 25)	4.41 (s.d. = 0.2)	99.95 (s.d. = 6.31)	1.114 (s.d. = 0.05)	(Estili et al., 2012)	11
	Silica glass	2.6	117 (s.d. = 60)	0.6 (s.d. = 0.1)	45 (s.d. = 23.08)	0.23 (s.d. = 0.04)	(Gao et al., 2017)	1
	SiC	3.2	338 (s.d. = 5)	3.5 (s.d. = 1.0)	105.6 (s.d. = 1.56)	1.09 (s.d. = 0.31)	(Bouville et al., 2014)	2
	Concrete	2.4	12	0.8 (s.d. = 0.6)	5 (s.d. = 0)	0.33 (s.d. = 0.25)	(Gao et al., 2017)	1
	Epoxy resin	1.17	58.46 (s.d. = 23)	2 (s.d. = 0.8)	51.28 (s.d. = 19.66)	1.03 (s.d. = 0.68)	(Gao et al., 2017)	1
	PU	0.82	30 (s.d. = 10)	0.25 (s.d. = 0.05)	36.59 (s.d. = 12.2)	0.3 (s.d. = 0.06)	(Bouville et al., 2014)	2
	Nylon	1.13	100 (s.d. = 10)	3.78 (s.d. = 1.6)	88.5 (s.d. = 8.8)	3.36 (s.d. = 1.42)	(Bouville et al., 2014)	2
	Cu-alloys	8.5	221 (s.d. = 136)	56.53 (s.d. = 29.33)	26 (s.d. = 16)	6.55 (s.d. = 3.45)	(Bouville et al., 2014)	2
	Fe-alloys	-	-	-	39.5 (s.d. = 20.5)	2.15 (s.d. = 0.95)	(Bouville et al., 2014)	2
	PS	1.05	50 (s.d. = 10)	0.9 (s.d. = 0.2)	47.62 (s.d. = 9.52)	0.86 (s.d. = 0.2)	(Bouville et al., 2014)	2
	CFRP	-	-	-	525 (s.d. = 175)	8.5 (s.d. = 4.5)	(Bouville et al., 2014)	2
	Al-SiC	-	-	-	115 (s.d. = 15)	7.15 (s.d. = 1.85)	(Bouville et al., 2014)	2
	GRPF	-	-	-	100 (s.d. = 25)	7.25 (s.d. = 3.75)	(Bouville et al., 2014)	2
	Ti-alloys	-	-	-	175 (s.d. = 115)	13.5 (s.d. = 4.5)	(Bouville et al., 2014)	2
	Steel				241.49 (s.d. = 76.58)	13.49 (s.d. = 2.03)	(Bouville et al., 2014)	2
	Mg alloys	-	-	-	140.68 (s.d. = 121)	8.95 (s.d. = 1.65)	(Bouville et al., 2014)	2
	metallic glass	-	-	-	250.48 (s.d. = 49.02)	19.92 (s.d. = 4.4)	(Bouville et al., 2014)	2
	our material	1.7	387 (s.d. = 40)	14.3 (s.d. = 1.8)	227.65 (s.d. = 23.53)	8.4 (s.d. = 1. 6)		

1
2

Transparent Methods

Materials

Aramid (Kevlar 49) fibers were purchased from DuPont Company. Potassium hydroxide (KOH), benzyldimethylamine (BDMA), and (3-Mercaptopropyl) trimethoxysilane was purchased from Aladdin Chemical Reagent Co. Polyacrylic acid (PAA) (Mw=250000) was purchased from Sigma-Aldrich. Methanol, 3-(trimethoxysilyl) propyl methacrylate (γ-MPS), (3-aminopropyl) trimethoxysilane, sodium hydroxide (NaOH), hydrochloric acid (HCl), sodium chloride (NaCl) and dimethyl sulfoxide (DMSO) were purchased from Sinopharm Chemical Reagent Co. Methyltetrahydrophthalic anhydride (MTHPA) and glycidyl ester were purchased from Tokyo Chemical Industry Co., Ltd. Mica microplatelets was obtained from Anhui Gerui Co. All chemicals were used without further purification.

Preparation of ANFs-Mica films

Aramid nanofibers (ANFs) solution (10 mg mL^{-1}) was prepared by dissolving aramid fibers (10 g) in DMSO (1 L) with 10 g KOH (Lyu et al., 2016). Mica microplatelets were modified with PAA (PAA-mica) according to a modified earlier work (Gole and Murphy, 2005). In a typical procedure, 10 g mica, 200 mg PAA and 584 mg NaCl were dispersed in 1 L deionized water (DIW), and then stirred for 1 h. After that, the PAA-mica was collected by centrifugation, followed by washing with DIW and DMSO for several times, and then dispersed into moderate amount of DMSO again. The desired amounts of ANFs and PAA-mica were mixed together by stirring for 20 min to ensure homogeneous dispersions. Consequently, the ANFs-Mica hydrogel was produced by spraying appropriate amount of dispersion on glass substrate at room temperature with ~50% relative humidity (RH), followed by immersing it into DIW (room temperature) for 6 h to exchange DMSO with DIW and further protonate ANFs, resulting in restoring the molecular structure of the ANFs. For a typical spraying conditions, the nozzle size is about 0.5 mm, air pressure from pneumatic pump is about 0.5 MPa, and the distance of the spray gun from the substrate is about 20 cm. The freestanding ANFs-Mica films were prepared by drying the ANFs-Mica hydrogel on a 60 °C heating stage for 6 h.

Fabrication of bulk composites

To fabricate the hierarchically ordered nacreous bulk material, these ANFs-Mica films were cut into equal-sized pieces, which were then heat treated at 120 ^{o}C for 4 h to remove extra moisture as possible. Subsequently, these pieces were stacked, and then pre-pressed with 15 MPa pressure at 60 °C for 6 h to eliminate the crimping deformation of the films and smooth them as possible, which is beneficial to stack them together for further hot-pressing. After the above processes, these pieces were immersed into 1 wt.% γ-MPS/methanol solution at 60 °C for 4 h (Bonderer et al., 2008). Then, they were impregnated into epoxy resin solution (weight ratio glycidyl ester/MTHPA/BDMA of 100:100:2) for 8 h at room temperature, and then laminated together (Cheng et al., 2012). After that, the stacked prepreg was hot-pressed with certain pressure (15, 30, or 60 MPa) at 120 °C for 72 h. The pure ANFs bulk composite was prepared via the same laminating process as described above. For disordered composite, the ANFs-Mica hydrogel was transformed into an aerogel by supercritical CO_2 drying. The aerogel was then processed as that for fabrication of the ordered bulk composite.

Sample characterizations

SEM (Zeiss Merlin Compact, 5 kV) were applied for characterizing the morphology and structure of the as-prepared samples. X-ray diffraction patterns were performed on a Philips X'Pert Pro Super X-ray diffractometer with Cu Ka radiation. Zeta potential values were measured by Malvern Nano-2590. Fourier transform infrared spectroscopy analysis was carried out on a Bruker Vector-22 spectrometer. Thermal gravimetric analysis (TGA) data was determined on a STA449F3 thermal analyzer with a heat rate of 10 °C min^{-1} in air. X-ray photoelectron spectroscopy tests were recorded on an X-ray photoelectron spectrometer using Mg Ka radiation exciting source (ESCALAB 250Xi). Transmittance and absorbance spectra were investigated by UV-2501PC/2550. Digital microscope (B011, Shenzhen D&F co., LTD, China) was used to capture the dynamic crack propagation of the nacreous bulk composite under the three-point bending test. The method of mass divided by volume was applied to calculate density of the bulk composites. UV radiation test of pure ANFs and 40 wt.% ANFs-Mica films were measured on accelerated ageing tester (Y/UVB-313) at 30 °C with 50% RH (ASTM G155). At least 6 films (~4 cm × 3 cm × 30 μm) and bulk beam specimens (~1.5 mm × 2 mm × 20 mm) with different UV radiation times were measured under same conditions, respectively. The thermal stability test of pure ANFs and 40 wt.% ANFs-Mica films (at least 6 pieces of specimens with size of ~4 cm × 3 cm × 30 μm) were conducted by storing them in muffle furnace under 200 ^{o}C, 250 ^{o}C and 300 ^{o}C for 6 h, respectively.

Mechanical testing

The mechanical tests (tensile and three-point bending tests) were measured by using Instron 5565A with 500 N load cells. For all these mechanical tests, at least six samples were evaluated at room temperature and ~50% RH, and then its average values were displayed. For tensile tests, strip specimens of a film (~3 cm × 3 mm × 30 μm) were measured at a loading rate of 1 mm min^{-1}. For three-point bending tests, beam samples of a bulk composite were carefully prepared with size of ~1.5 mm × 2 mm × 20 mm, which was measured at a loading speed of 0.2 mm min^{-1}. For single-edge notched bending (SENB) tests, the beam specimens (~3 mm × 3 mm × 20 mm) were first notched by using 150 μm-thick diamond raw to ~1.5 mm (half of their width), and the notch roots were then sharpened to their radius of ~50 μm by a razor blade. A constant loading rate of 1 μm s^{-1} was chosen to carry out at the tests. Vickers hardness tests were performed by using microhardness tester (DuraScan-70, Dantsin, Switzerland). The applied loading direction was perpendicular to the basal surface of mica microplatelets in all vickers hardness and three-point bending tests.

Calculation of fracture toughness

Fracture toughness, K_{IC}, was calculated by following equations: (Bouville et al., 2014; Gao et al., 2017; Mao et al., 2016)

$$K_{IC} = \frac{P_{Ic} S}{B W^{3/2}} f(a/W) \tag{1}$$

$$f(a/W) = \frac{3(a/W)^{1/2}[1.99 - (a/W)(1-a/W)(2.15 - 3.93a/W + (a/W)^2)]}{2(1+2a/W)(1-a/W)^{3/2}} \tag{2}$$

Where, P_{Ic} is the maximum load in SENB experiment, *S* is support span, and *B*, *W* and *a* are the thickness, width, and notch depth of the beam specimen, respectively.

Fracture toughness, K_{JC}, was obtained by exploiting *J*-integral calculation to calculate the elastic and plastic contribution, resembling earlier method to examine the mechanical properties of other natural and artificial bulk composite materials: (Bouville et al., 2014; Gao et al., 2017; Mao et al., 2016; Munch et al., 2008; Naglieri et al., 2015)

$$J = J_{el} + J_{pl} \tag{3}$$

J_{el} is the elastic contribution on account of linear elastic fracture mechanics:

$$J_{el} = \frac{K_{IC}^{\ 2}}{E'} \tag{4}$$

On the other hand, the plastic contribution, J_{pl}, can be calculated from the follow equation:

$$J_{pl} = \frac{2A_{pl}}{B(W-a)} \tag{5}$$

In which, A_{pl} is the plastic area underneath the load-displacement curve.

Therefore, *J* values can be processed into *K* values with the follow equation:

$$K_{JC} = (JE')^{1/2} \tag{6}$$

In which, $E' = E(1-\nu^2)$, *E* and *v* are Young's modulus poisson's ratio, respectively. Because K_{Jc} is affected by the variation of *E* in a fairly limited way, here, E' can be replaced with *E*.

Crack extension value, Δa, was calculated on the basis of earlier recursion method by the follow equations: (Bouville et al., 2014; Gao et al., 2017; Mao et al., 2016)

$$a_n = a_{n-1} + \frac{W - a_{n-1}}{2} \frac{C_n - C_{n-1}}{C_n} \tag{7}$$

$$C_n = u_n / f_n \tag{8}$$

$$\Delta a = a_n - a \tag{9}$$

In which, a_n, C_n, u_n and f_n are the crack length, complaisance, displacement, and loading force calculated at each point after the creak departure, respectively. *W* is the width of the specimen.

Theoretical analysis of toughening mechanisms of the nacreous ANFs-Mica bulk

The fracture toughness *(K_{JC})* for the nacreous structure under far-field tensile stress *(σ_∞)* is expressed as

$$K_{JC} = K_{IC} + \Delta K_{br} \tag{10}$$

where K_{JC} corresponds to the actual fracture toughness measured experiments, K_{IC} characterizes the intrinsic fracture toughness induced by micro-damage around crack tip (Ritchie, 2011). ΔK_{br} denotes the increase of the stress intensity factor due to the platelet bridging mechanism (Budiansky and Amazigo, 1989)

$$\Delta K_{br} = \sqrt{2/\pi}\int_0^{\lambda}[\sigma_b(x)/\sqrt{\lambda - x}]dx \tag{11}$$

Based on the shear-lag model (Cox, 1952; Gao et al., 2003), the tensile stress $\sigma_b(x)$ of the mica microplatelets at coordinate *x* in the crack bridging zone can be written as

$$\sigma_b(x) = \phi\tau_{\max}[l - 2\delta(x)]/t_b \tag{12}$$

where ϕ is the volume fraction of the mica, *l* and t_b are the length and thickness of mica platelet, respectively. $\delta(x)$ stands for the crack opening displacement at coordinate *x* in the crack bridging zone. The maximum pullout length of a platelet is half of the platelet length, which corresponds to the maximum crack opening displacement. $\tau_{\max}$ represents the shear cohesive strength of the crosslinked interface, which depends primarily on the density of hydrogen bonds networks in the interlayer ANFs (Chowdhury and Gillespie, 2018; Wu et al., 2018).

Based on Eqs. (11) and (12), the fracture toughness can be calculated as

$$K_{JC} = K_{IC} + 2\phi\tau_{\max}\left\{\sqrt{\lambda}l - \int_0^{\lambda}[\delta(x)/\sqrt{\lambda - x}]dx\right\}/(\pi t_b) \tag{13}$$

The crack opening displacement $\delta(x)$ for the mode-I semi-infinite crack in isotropic materials can be calculated by (Budiansky and Amazigo, 1989; Meng et al., 2017)

$$\begin{aligned}\delta(x) = {} & 8K_{JC}\sqrt{\lambda - x}/\sqrt{2\pi}E \\ & - 4\{\int_0^{\lambda}\sigma_b(\alpha)\ln[(\sqrt{\lambda - x} + \sqrt{\lambda - \alpha})/(\left|\sqrt{\lambda - x} - \sqrt{\lambda - \alpha}\right|)]d\alpha\}/(\pi E)\end{aligned} \tag{14}$$

Theoretical analysis of the effect of platelet volume fraction on the mechanical properties of nacreous ANFs-Mica film.

During the pullout process of a platelet in the nacreous ANFs-Mica bulk, its interfacial stress retains the constant τ_f due to the reformation of hydrogen bonds at the interfaces. Therefore, in Figures S12A and S12B, we adopt a shear-lag model considering an elastic-perfectly plastic interface constitutive relation to analyse the toughening mechanisms of the nacreous structure (Ni et al., 2015; Sakhavand and Shahsavari, 2015). The interfacial plasticity could be represented by a dimensionless parameter $C = \left(\delta_f - \delta_y\right)/\delta_y$, where δ_y denotes the yielding strain and δ_f. Previous work of N Sakhavand et al (Sakhavand and Shahsavari, 2015) shows that the normalized dimensionless mechanical properties (the effective strength $\bar{\sigma}_c$ and toughness $\bar{T}_c$) as a function of volume fraction can be calculated as

$$\begin{cases} \bar{\sigma}_c = \dfrac{\sigma_c}{\tau_f} = \dfrac{\sqrt{(1-\phi)\phi}}{\beta\sqrt{t_b}}\, f_\sigma\left(\dfrac{\beta}{\sqrt{t_b}}\sqrt{\dfrac{\phi}{1-\phi}}l\right) \\ \bar{T}_c = \dfrac{T_c}{\tau_f^2/G} = (1-\phi)\, f_T\left(\dfrac{\beta}{\sqrt{t_b}}\sqrt{\dfrac{\phi}{1-\phi}}l\right) \end{cases} \tag{15}$$

where $\phi = t_b/(t_b+h)$ is defined as the volume fraction of the mica platelets; t_b, l, E are the thickness, the length and the Young's modulus of platelets, respectively; $\beta = \sqrt{G/(Et_b)}$ is a parameter denoting the interface properties (G is shear modulus); f_σ, f_T are the dimensionless functions representing normalized strength and toughness, and the detailed calculations can be seen in reference (Sakhavand and Shahsavari, 2015).

In this work, a typical value of interfacial plasticity C = 2 was adopted, the strength and toughness can be calculated using Eq. (15). The mechanical properties as a function of platelet volume fraction are shown in Figures S12C and S12D. Strength and toughness first increase with the volume fraction and then decrease, i.e., there exist optimum volume fractions that maximize the strength and toughness. This model assumes that the interface only tolerate shear failure and cannot tolerate tension strain. As ϕ is increased, more platelets bear the tension load, which results in the incensement of the strength and toughness. At the optimum ϕ, the load is optimally transferred between the platelets via the shear strain of the interface to provide the maximum strength and toughness. By further increasing ϕ, less and less matrix are present to transfer the load until ϕ = 100% where the applied load will only cause rigid body motion of the platelets without load transfer to each other, thus the strength and toughness decreases. It's worth mentioning that the values of optimum volume fractions depend on material and geometry parameters, the detailed analyses can be found in (Sakhavand and Shahsavari, 2015).

FE simulation of the nacreous ANFs-Mica bulk under three-point bending

A 3D FE model of the nacreous structure with interlayer nonlinear sliding is developed using the commercial software ABAQUS v6.14, as shown in Figure S20A. In the simulation, we constructed a 3D nacreous structure (250 × 60 × 2 μm^3) with a single-edge notch (2 × 4 × 2 μm^3). The model contains randomly staggered arrangement of stiff platelets bonded by soft interlayer biopolymer with zero thickness. The mica platelets with isotropic bulk modulus E = 20 GPa and Poison ratio v = 0.33 undergo elastic deformation before brittle failure. During the pullout process of a mica platelet in the nacreous ANFs-Mica bulk, its interfacial stress retains the constant τ_f due to the reformation of hydrogen bonds at the interfaces. Therefore, the interlayer biopolymer is model as a cohesive zone with a trapezoidal cohesive law, which can control the sliding and softening by defining the size of the traction plateau. As shown in Figure S20B, the key input parameters of the trapezoidal cohesive law were the fracture energy (G_c), the interfacial strength (τ_f), the initial stiffness ($K = \tau_f/\delta_y$) and a ratio ($r = (\delta_I - \delta_y)/\delta_f$) governing the shape of the traction-separation relation.

$$\tau_f = (1-d)k\delta \tag{16}$$

In ABAQUS, the cohesive traction response is defined through damage variable d, i.e.

The damage evolution for a monotonically increasing δ takes the form of the equation below:

$$d = \begin{cases} 0 & 0 \le \delta \le \delta_y \\ 1-\tau_f/(K\delta) & \delta_y \le \delta \le \delta_I \\ 1-\left[\tau_f/(K\delta)\right]*\left[(\delta_f-\delta)/(\delta_f-\delta_I)\right] & \delta_I \le \delta \le \delta_f \\ 1 & \delta \ge \delta_f \end{cases} \tag{17}$$

A user subroutine, user-defined mechanical material behavior for standard analysis (UMAT), was developed to implement the trapezoidal cohesive model for the interlayer crosslink in which the shear strength and the modulus are 200 MPa and 5 GPa, respectively. The mix mode behavior was assumed mode-independent and

the critical fracture energy is 20 N/m. A typical ratio $r = 0.35$ was adopt in the trapezoidal cohesive law to consider the plasticity due to the reformation of hydrogen bonds at the interfaces in the nacreous ANFs-Mica bulk. The model under three-point bending was constructed to simulate the crack propagation.

Supplemental References

Alkilany, A.M., Nagaria, P.K., Hexel, C.R., Shaw, T.J., Murphy, C.J., and Wyatt, M.D. (2009). Cellular uptake and cytotoxicity of gold nanorods: molecular origin of cytotoxicity and surface effects. Small *5*, 701-708.

Bonderer, L.J., Studart, A.R., and Gauckler, L.J. (2008). Bioinspired design and assembly of platelet reinforced polymer films. Science *319*, 1069-1073.

Cheng, Q.F., Li, M.Z., Jiang, L., and Tang, Z.Y. (2012). Bioinspired layered composites based on flattened double-walled carbon nanotubes. Adv Mater *24*, 1838-1843.

Chowdhury, S.C., and Gillespie, J.W. (2018). A molecular dynamics study of the effects of hydrogen bonds on mechanical properties of Kevlar (R) crystal. Comput Mater Sci *148*, 286-300.

Cox, H.L. (1952). The elasticty and strength of paper and other fibrous materials. Br J Appl Phys *3*, 72-79.

Gao, H.J., Ji, B.H., Jäger, I.L., Arzt, E., and Fratzl, P. (2003). Materials become insensitive to flaws at nanoscale: lessons from nature. Natl Acad Sci USA *100*, 5597-5600.

Gole, A., and Murphy, C.J. (2005). Polyelectrolyte-coated gold nanorods: Synthesis, characterization and immobilization. Chem Mater *17*, 1325-1330.

Guan, Y., Li, W., Zhang, Y.L., Shi, Z.Q., Tan, J., Wang, F., and Wang, Y.H. (2017). Aramid nanofibers and poly (vinyl alcohol) nanocomposites for ideal combination of strength and toughness via hydrogen bonding interactions. Compos Sci Technol *144*, 193-201.

Jia, F.F., and Song, S.X. (2014). Exfoliation and characterization of layered silicate minerals: a review. Surf Rev Lett *21*, 1430001.

Lyu, J., Wang, X.Z., Liu, L.H., Kim, Y., Tanyi, E.K., Chi, H., Feng, W.C., Xu, L.Z., Li, T.H., Noginov, M.A.*, et al.* (2016). High strength conductive composites with plasmonic nanoparticles aligned on aramid nanofibers. Adv Funct Mater *26*, 8435-8445.

Ma, Z., Kang, S., Ma, J., Shao, L., Wei, A., Liang, C., Gu, J., Yang, B., Dong, D., Wei, L.*, et al.* (2019). High-performance and rapid-response electrical heaters based on ultraflexible, heat-resistant, and mechanically strong aramid nanofiber/Ag nanowire nanocomposite papers. ACS Nano *13*, 7578-7590.

Meng, Q.H., Li, B., Li, T., and Feng, X.Q. (2017). A multiscale crack-bridging model of cellulose nanopaper. J Mech Phys Solids *103*, 22-39.

Ni, Y., Song, Z.Q., Jiang, H.Y., Yu, S.H., and He, L.H. (2015). Optimization design of strong and tough nacreous nanocomposites through tuning characteristic lengths. J Mech Phys Solids *81*, 41-57.

Sakhavand, N., and Shahsavari, R. (2015). Universal composition-structure-property maps for natural and biomimetic platelet-matrix composites and stacked heterostructures. Nat Commun *6*, 6523.

Si, L.M., Lu, Z.Q., Yao, C., Ma, Q., Zhao, Y.S., Wang, Y.F., Wang, D.N., and Jin, Z.F. (2020). Nacre-like nanocomposite film with excellent dielectric insulation properties and mechanical strength based on montmorillonite nanosheet and aramid nanofiber. J Mater Sci *55*, 5948-5960.

Wat, A., Lee, J.I., Ryu, C.W., Gludovatz, B., Kim, J., Tomsia, A.P., Ishikawa, T., Schmitz, J., Meyer, A., Alfreider, M.*, et al.* (2019). Bioinspired nacre-like alumina with a bulk-metallic glass-forming alloy as a compliant phase. Nat Commun *10*, 961.

Wu, K.J., Song, Z.Q., He, L.H., and Ni, Y. (2018). Analysis of optimal crosslink density and platelet size insensitivity in graphene-based artificial nacres. Nanoscale *10*, 556-565.

Zhu, J.Q., Cao, W.X., Yue, M.L., Hou, Y., Han, J.C., and Yang, M. (2015). Strong and stiff aramid nanofiber/carbon nanotube nanocomposites. ACS Nano *9*, 2489-2501.